Department of Precision and Microsystems Engineering

TIP IDENTIFICATION IN ATOMIC FORCE MICROSCOPY USING NONLINEAR DYNAMICS

Thomas Gribnau

Report no	: 2017.058
Coach	: Dr. ir. F. Alijani & Ir. E. Rull Trinidad
Professor	: Prof. dr. U. Staufer
Specialisation	: Micro & Nano Engineering (MNE)
Type of report	: MSc Thesis
Date	: December 4, 2017

Delft University of Technology

Challenge the future

Tip identification in Atomic Force Microscopy using nonlinear dynamics

by

Thomas Gribnau

to obtain the degree of

Master of Science
in Mechanical Engineering

at the Delft University of Technology,
to be defended publicly on Monday December 4, 2017 at 9:30 AM.

Student number:	4094387	
Supervisors:	Prof. dr. U. Staufer,	TU Delft
	Dr. ir. F. Alijani,	TU Delft
	Ir. E. Rull Trinidad.	TU Delft
Thesis committee:	Prof. dr. ir. P. G. Steeneken,	TU Delft
	Dr. ir. F. Alijani,	TU Delft
	Ir. J. W. Spronck,	TU Delft
	Ir. E. Rull Trinidad.	TU Delft

An electronic version of this thesis is available at `http://repository.tudelft.nl/`.

Preface

A little over a year ago I started this thesis project and to finally write the last words of this report feels very good. I'm proud of the work, and I couldn't have done it without the support of many people. I especially want to thank Farbod, Urs, Enrique and Pierpaolo for all their help, supervision and contribution to this project. It is very rewarding that we managed to publish after all the hard work, and it most surely compensates for all the long hours Enrique and I have spent in the lab. Finally, I want to thank my family, friends and fellow students for all the good times and making this year the best of my student life.

Thomas Gribnau
Delft, December 2017

Abstract

Since its invention, the Atomic Force Microscope (AFM) has emerged into one of the most useful tools in nanotechnology due to its acclaimed abilities in exploring surface topography, micro- and nanoscale manipulation and characterization. The nonlinear interaction between the cantilever tip and the sample surface has been studied in great detail and a thorough understanding of the cantilever dynamics can improve measurements and lead to new methods for identification, manipulation and characterization. One of the biggest challenges in the field of AFM is related to the identification of the cantilever tip size. The accuracy of measurements in AFM is directly related to the size and geometry of this tip. It is desired that the tip condition can be continuously monitored in between or even throughout measurements in order to provide high quality measurements. In this thesis project, a methodology for tip assessment is introduced based on the nonlinear dynamic response of the cantilever. The method consists of the acquisition of frequency response curves in the attractive regime where the influence of the tip radius is predominant. Experimental frequency response curves are fitted to the tip-sample interaction model that includes the van der Waals forces. It is found that exploiting the nonlinear dynamic response of the cantilever is a safe and accurate method for tip assessment.

Contents

List of Figures ix

List of Tables xiii

1 A Brief Introduction to AFM 1

1.1 The AFM System . . . 2
1.2 Amplitude Modulation Atomic Force Microscopy . . . 3
1.3 Previous Research on Tip Identification . . . 4
1.3.1 Tip Estimation with Electron Microscopy . . . 4
1.3.2 'Blind Tip Reconstruction' . . . 4
1.3.3 Exploiting the Tip-Sample Interaction . . . 4
1.4 Research Question & Strategy . . . 5

2 Mechanics of the Tip-Sample Interaction 7

2.1 The Tip-Sample Interaction Potential . . . 7
2.2 The Lennard-Jones Potential . . . 8
2.3 Long-Range Interaction Forces . . . 8
2.4 Short-Range Repulsive Forces . . . 10
2.4.1 The Hertz Model . . . 10
2.4.2 The DMT Model . . . 10
2.4.3 The JKR Model . . . 10
2.5 Electrostatic & Capillary Forces . . . 11
2.6 Interaction Model Selection . . . 11

3 Nonlinear Cantilever Dynamics in AM-AFM 13

3.1 Equation of Motion . . . 13
3.2 Coexistence of Multiple Oscillation States . . . 14
3.3 Higher Modes & Higher Harmonics . . . 15

4 Experimental Methodology 17

4.1 Experimental Setup . . . 17
4.1.1 The AFM Scanner and Controller . . . 17
4.1.2 The Multi-Frequency Lock-In Amplifier . . . 17
4.1.3 Experimental Environment, Conditions & Considerations . . . 18
4.2 Probing the Attractive Forces . . . 18
4.2.1 Attractive Forces & Higher Harmonics . . . 19
4.2.2 Influence of Attractive Forces on the Frequency Response . . . 20
4.3 Experimental Procedure . . . 22
4.3.1 Procedure 1: 'Tip Lift' . . . 22
4.3.2 Procedure 2: 'Z-Axis Closed-Loop-Control' . . . 24
4.4 Identification Process . . . 25
4.5 Validation with SEM . . . 26

5 Results 27

5.1 Experiment 1 . . . 27
5.2 Experiment 2 . . . 28

6 Discussion 29

6.1 Evaluation of the Results . . . 29
6.2 Validation of the Method . . . 29

7 Recommendations & Conclusion **31**
7.1 Recommendations 31
    7.1.1 Implementation of a Nonlinear System Identification Algorithm. 31
    7.1.2 Exploiting Higher Harmonics & Intermodulation Products 31
    7.1.3 True Tip Shape Determination 31
    7.1.4 Future Research and Outlook 32
7.2 Conclusion 32

A Analytical Descriptions **33**
A.1 Dimensionless Equation of Motion 33
A.2 Nonlinear Identification Algorithm 35
    A.2.1 Approximated Solution Using a Truncated Taylor Series 35
    A.2.2 Analytical Solution 36

B Additional Results **37**
B.1 Contamination of AFM Tips. 37
    B.1.1 Experiments on a Mica Sample 37
    B.1.2 Experiments on a HOPG Sample 38
B.2 Frequency Spectrum of the FMR Cantilever in Different Operating Conditions 39
B.3 Higher Harmonic Imaging 40
B.4 Fitting Results 41
    B.4.1 Experiment 1. 41
    B.4.2 Experiment 2. 41
B.5 Irregularities in the Frequency Response 42
B.6 Backbone Curves Indicating Drift in z_c 42

C Supplementary Information **43**
C.1 Preparing an Experiment 43
    C.1.1 Cantilever Mounting 43
    C.1.2 Laser Alignment 43
    C.1.3 Calibrations 45
C.2 Cantilever Specifications 46

Bibliography **47**

List of Figures

1.1 Schematic representation of the AFM set-up. In this configuration the actuator is attached to the probe stage and is moved over the stationary sample surface (source: FLEX AFM operating manual). 2
1.2 Frequency response, simulated for a Single Degree Of Freedom (SDOF) harmonic oscillator when it is excited just above resonance (solid line) and under influence of attractive and repulsive forces (dashed lines). Without any external force the system is excited just above resonance (dotted line) at ω_d. 3

2.1 The AFM force potential, which the force-distance relation between tip and sample, the contact (blue) and noncontact (magenta) regions are indicated. A is a point on the force potential where the cantilever is far away from the sample and barely affected by the attractive forces. B is a point closer to the sample, where the cantilever experiences an attractive force. C is a point where there is contact between tip and sample and the net force on the cantilever is repulsive. . 7
2.2 Schematic of the AFM and the sample surface. The rest position of the cantilever acts as reference for its deflection z. This figure is adopted from the publication in Applied Physics Letters [1]. 8
2.3 Plot of the force-distance relation for different tip geometries, visualizing the difference in the van der Waals forces between a (hemi-)spherical ($R = 10\,\mathrm{nm}$), flat-circular ($r = 10\,\mathrm{nm}$) and conical tip ($\theta = 20°$). Cantilever and material properties are kept constant throughout the simulations. 9
2.4 A series of force-distance curves for a (hemi-)spherical tip shape, for increasing values of the tip radius R. 9
2.5 Force-distance relations for the different contact models. LEFT: Hertzian contact, describing repulsive interaction at zero separation. MIDDLE: DMT model, where a transition from attractive to repulsive interaction occurs at $d = a_0$. RIGHT: JKR model, where the effect of adhesion is incorporated. Hysteresis is observed between the approach and retract phase. 11
2.6 Water capillary bridge that is formed between tip and sample, observed in an SEM. The water bridge was obtained by drastically increasing the relative humidity (RH > 98 %). Adopted from [2]. 11

3.1 Experimental A-d curve (approach and retract phase) taken on a mica sample. Partial sections of the high and low amplitude branches are observed. A is the point in the approach phase where a transition from the low to the high amplitude branch occurs. B is the point in the retract phase were a transition from the high to the low amplitude branch takes place. Adopted from [3]. 14
3.2 Numerical simulations of a nonlinear SDOF harmonic oscillator, demonstrating bi-stability and hysteresis in the frequency response when subjected to attractive and/or repulsive forces. The backbone curves are illustrative and not obtained with numerical simulations (black dashed line). LEFT: Exclusively attractive interaction. Experimentally, because an unstable solution (black dotted line) cannot be obtained, at the saddle-node point (black dot) a jump from one to the other stable branch takes place (arrow). For very small oscillations the resonance can be approximated by a linear oscillator. MIDDLE: Purely repulsive interaction, showing similar behaviour in the other direction. RIGHT: Result of an attractive-repulsive potential on the frequency response curve, showing both softening and hardening. 15
3.3 Experimental frequency spectrum of an AFM cantilever during tapping mode operation. The highest red line signifies the location of the driving frequency and the other red lines mark the integer multiples, i.e. harmonics. 15

4.1 Overview of the complete experimental set-up placed on a vibration isolation platform. From left to right: the FLEX AFM scanner, the signal acquisition module or breakout box, the C3000 controller and the multi-frequency lock-in amplifier. 17

4.2 Overview of the connections between the AFM, controller, signal acquisition module (SAM) and MLA. The red line marks the photodetector signal, the green lines represent the EOL and EOF triggers and the black line the cantilever drive signal (source: `http://www.intermodulation-products.com/`). . . . 18

4.3 The AFM scanner surrounded by Petri dishes filled with dry silica. In this picture the chamber was removed, hence the humidity is immediately increased to 13 %, indicated by the sensor. . . 18

4.4 Experimental frequency spectra of an FMR cantilever interacting with a mica sample at different amplitude reduction set-points. The frequency and amplitude are normalized with respect to the driving frequency $\omega_\mathrm{d} = 71.7\,\mathrm{kHz}$. . . . 19

4.5 Experimental dynamic approach measurement where the driving frequency and several higher harmonics are tracked simultaneously, starting from $z_\mathrm{c} \approx 50\,\mathrm{nm}$ until the sample is reached ($z_\mathrm{c} \approx 0\,\mathrm{nm}$). The dashed line marks the transition from attractive to repulsive regime. The signals are normalized with respect to the free vibration amplitude of the drive frequency $\omega_\mathrm{d} = 163.7\,\mathrm{kHz}$. . . . 20

4.6 Simulated frequency response curve of a SDOF harmonic oscillator, turning from softening into hardening. The experimental forward sweep gives as a solution the blue lines. The remaining parts of the stable solutions, coloured red, can be obtained by performing a backward sweep. The unstable solutions cannot be found experimentally. . . . 21

4.7 Frequency response for different values of the tip radius R (from blue to yellow $R = \{10, 130\}\,\mathrm{nm}$). For the numerical simulation, $z_\mathrm{c} = 20\,\mathrm{nm}$ and a Hamaker constant between a Silicon (Si) tip and a Highly Oriented Pyrolytic Graphite (HOPG) sample $H_{\mathrm{Si-HOPG}} = 2.9656 \times 10^{-19}\mathrm{J}$ was considered. This figure is adopted from a publication in Applied Physics Letters, for which I have performed the numerical simulations [1]. . . . 21

4.8 The available imaging modes in the AFM. The operating modes consist of a forward (1) and a backward (2) scan. The standard mode follows the sample in both the first and second scan. The dual scan mode allows the user to follow a slope or the sample contour during the second scan. With the interlaced mode the forward and backward scan can be decoupled. In the second scan only, the surface is found with the first scan, and the second scan is carried out following a slope. 22

4.9 Experimental backbone curve obtained with the 'tip lift' procedure, performed on a mica sample, $z_\mathrm{c} \approx 30\,\mathrm{nm}$. The color code indicates an increase in excitation. . . . 23

4.10 Multiple forward (blue) and backward (red) sweeps performed with the 'tip lift' procedure and a constant driving force. . . . 23

4.11 Experimental frequency response curve with increasing excitation amplitude. The color code indicates an increase in excitation (2 mV steps were made). The solid line indicates the backbone curve, and the sample is at $z_\mathrm{c} = 20\,\mathrm{nm}$. This figure is adopted from a publication in Applied Physics Letters [1]. The experiments have been performed by E. Rull Trinidad and myself. . . . 24

4.12 Branch diagram, visualising the brute force fitting procedure, starting from the optimal fit S_{z_c,F_0}. In a typical fitting procedure 4 values for Q are found where the saddle node points can be matched properly. Often, more than 60 simulation iterations are performed before a single fitting procedure is completed. . . . 25

4.13 SEM image of the cantilever tip. The proposed circular fit follows the part the tip that interacts with the sample. . . . 26

4.14 SEM image of an AFM tip with contamination at its sharp end. . . . 26

5.1 LEFT: Forward (blue dots) and backward (red dots) experimental frequency response curves with a proposed numerical fitting (black line) of $R = 19\,\mathrm{nm}$. The small inset graph targets the saddle node points (light blue dots) and contains simulated curves of the upper and lower bound retrieved from the fitting. RIGHT: SEM image of the corresponding AFM tip. The numerical simulation for $R = 19\,\mathrm{nm}$ was performed with $Q = 387$, $F_0 = 1.325\,\mathrm{nN}$, $z_\mathrm{c} = 20\,\mathrm{nm}$, $\omega_\mathrm{n} = 166\,878\,\mathrm{Hz}$ and $k_\mathrm{c} = 26\,\mathrm{N\,m^{-1}}$. . . . 27

5.2 LEFT: Forward (blue dots) and backward (red dots) experimental frequency response curves with a proposed numerical fitting (black line) of $r = 12\,\mathrm{nm}$. The small inset graph targets the saddle node points (light blue dots) and contains simulated curves of the upper and lower bound retrieved from the fitting. RIGHT: SEM image of the corresponding AFM tip. The numerical simulation for $r = 12\,\mathrm{nm}$ was performed with $Q = 312$, $F_0 = 1.95\,\mathrm{nN}$, $z_\mathrm{c} = 25\,\mathrm{nm}$, $\omega_\mathrm{n} = 164\,973\,\mathrm{Hz}$ and $k_\mathrm{c} = 25.3\,\mathrm{N\,m^{-1}}$. . . . 28

A.1 Free body diagram of the AFM cantilever and the sample. The rest position of the cantilever acts as a reference for the deflection z. 33

B.1 Two SEM images taken from different sides of the cantilever used in the experiments on the mica sample. The left image shows a clear patch of contamination on the tip. The right image reveals that the tip is blunted. 37
B.2 SEM images of the cantilever contaminated with a patch of contamination and larger flakes of HOPG. 38
B.3 Cleaving of graphite (source: FLEX AFM operating manual). 38
B.4 Experimental frequency spectra of the same FMR cantilever used for the experiment in Fig. 4.4, whilst it scans a sample in the static mode, in the dynamic mode and in free air dynamically. . . 39
B.5 AM-AFM topography images of PS-LDPE of the driven frequency and several of the higher harmonics. The feedback was performed on the amplitude of ω_d. The higher harmonic images clearly show contrast between the two materials. 40
B.6 AM-AFM topography images of PS-LDPE of the driven frequency and its sixth harmonic. One of the scanning lines is highlighted to show the change in the amplitude for both cases. Where the amplitude of ω_d is monitored by the feedback, the amplitude of $6\omega_\mathrm{d}$ is free to change. 40
B.7 Experimental forward (blue dots) and backward (red dots) frequency response curves of two different NCLR cantilevers with softening nonlinearity. The height and width of these curves are difficult to fit, due to the discrepancy between the outer parts of the curves. 42
B.8 Experimental backbone curve obtained with the 'tip lift' procedure, performed on a mica sample, $z_\mathrm{c} \approx 30\,\mathrm{nm}$. The backbone indicates that the cantilever base moves away from the sample . 42
B.9 Experimental backbone curve obtained with the 'tip lift' procedure, performed on a mica sample, $z_\mathrm{c} \approx 30\,\mathrm{nm}$. The backbone indicates that the cantilever base moves towards the sample in the repulsive regime. 42

C.1 LEFT: Correct alignment of the cantilever chip on the holder. CENTER & RIGHT: Incorrect alignment (source: FLEX AFM operating manual). 43
C.2 Aligning the laser on the cantilever should start from the base edge (green area), followed by lateral centering on the cantilever (blue dot), and should finish near the tip end (orange dot)(source: FLEX AFM operating manual). 43
C.3 Schematic top view of the FLEX AFM, indicating the 4 holes with the screws, which can be adjusted to align the laser (source: FLEX AFM operating manual). 44
C.4 The laser alignment dialog, displaying the current position of the laser spot on the detector (green dot) (source: FLEX AFM operating manual). 44
C.5 Thermal tuning dialog of the controller software. 45
C.6 Thermal tuning dialog of the MLA. 45
C.7 Specification sheets of the AFM cantilevers used in this work, LEFT: FMR cantilever. RIGHT: NCLR cantilever (source: `https://www.nanoandmore.com/`. 46

List of Tables

2.1 Van der Waals interaction force derived for common tip-sample geometries, where R is the sphere radius, r is the radius of the flat-circular area and θ is the cone angle. Adapted from [4]. 9

B.1 Results of the numerical fitting procedure of the first experiment, discussed in section 5.1. LEFT: $z_\mathrm{c} - 1 = 19\,\mathrm{nm}$, MIDDLE: $z_\mathrm{c} = 20\,\mathrm{nm}$, RIGHT: $z_\mathrm{c} + 1 = 21\,\mathrm{nm}$. The tip radii for which a good fit of the saddle node points was obtained are colored green. The tip radii colored red provided a good fit for saddle node B, but saddle node A and the nonlinear part of the curve could not be fitted properly. 41

B.2 Results of the numerical fitting procedure of the second experiment, discussed in section 5.2. LEFT: $z_\mathrm{c} - 1 = 24\,\mathrm{nm}$, MIDDLE: $z_\mathrm{c} = 25\,\mathrm{nm}$, RIGHT: $z_\mathrm{c} + 1 = 26\,\mathrm{nm}$. The tip radii for which a good fit of the saddle node points was obtained are colored green. The tip radii colored red provided a good fit for saddle node B, but saddle node A and the nonlinear part of the curve could not be fitted properly. 41

1

A Brief Introduction to AFM

Since its invention in 1986 by Binnig et al., the Atomic Force Microscope (AFM) has emerged as a powerful instrument for various techniques like surface mapping, nanoscale manipulation, modification and characterization [5–9]. Due to its ability in gaining atomic resolution, the AFM has been widely used in chemistry, microbiology and engineering [10–12]. Over the years, a variety of AFM operating modes have been introduced, each suitable for different purposes.

In AFM, a microcantilever with a nanoscale tip attached to its end interacts with a nonlinear potential, consisting of both attractive and repulsive parts. Additional nonlinearities can be induced by adhesion, electrostatic or magnetic forces.

The operating modes of AFM can be categorized into static mode, when the AFM cantilever does not vibrate during measurement, and dynamic mode, where the cantilever is excited to vibrate at or near its resonance frequency. Dynamic AFM could either be amplitude modulation AFM (AM-AFM) or frequency modulation AFM (FM-AFM). Usually, AM-AFM is referred to as intermittent contact or tapping mode, and is characterized by the close proximity of the tip to the sample surface, which induces both attractive and repulsive interactions between the tip and sample atoms depending on their mutual distance [13]. Measurements can be performed by utilizing solely repulsive (contact mode) or attractive interaction between tip and sample (noncontact mode) [14].

Over time, AM-AFM has become the universally used mode for imaging due to the minimal interaction with the sample and the ease of use whilst maintaining the ability to obtain high resolution images. Since then, the mechanics of AM-AFM have been widely investigated. The nonlinear interaction between the cantilever tip and the sample surface has been studied broadly, but many aspects remain not fully explained. Typically, continuum elasticity based theories such as the Hertz, Johnson-Kendall-Roberts, and the Derjaguin-Muller-Toporov approximation are able to describe the tip-sample interaction [15–17]. These models are based on continuum mechanics and cannot provide information on the atomic scale. Their feasibility depends on the atomic structure of both tip and sample [18].

The multi-stable behaviour as a result of the nonlinear tip-sample interaction can lead to negative implications on the measurement. A thorough understanding of the nonlinear dynamics involved in AFM and especially AM-AFM can improve measurement quality and might lead to new methods for identification, manipulation and characterization.

The resolution that can be achieved with AM-AFM is directly related to the tip geometry [19, 20]. In the AFM field, the tip size is quantified by its radius of curvature, which could undergo alterations due to repeated mechanical contact with the surface. It has been pointed out that obtaining a method for precise tip size calibration is difficult [21, 22]. Many techniques have been presented to quantify the tip radius, but most of these come with an increased risk of tip damage and contamination. Therefore, an accurate and safe *in-situ* estimation of the tip radius remains an open research question.

1.1. The AFM System

In its essence an AFM is a system that uses a microsized cantilever to measure surfaces of samples. The most sensitive part of the cantilever is the nanoscale tip that is attached to its far end, which is the only part that interacts directly with the sample. Most of these cantilevers are constructed from Silicon (Si). The properties of both cantilever and tip have great influence on the sensitivity, repeatability and the resolution of topography imaging.

AFM probes are commonly shaped as rectangular cantilevers. In general, they need to be compliant enough to be deflected at very small force levels and the tip size needs to be comparable with the typical feature size of the sample in order to obtain accurate measurements. For each operating mode, specific cantilevers have been designed. The force constant of AFM cantilevers often needs to be calibrated in order to find its correct value. The force constant has a cubic dependency on the cantilever thickness, small irregularities and have a significant effect on the stiffness. Therefore, non-destructive procedures for calibrating the force constant of AFM cantilevers *in-situ* have been developed [23, 24].

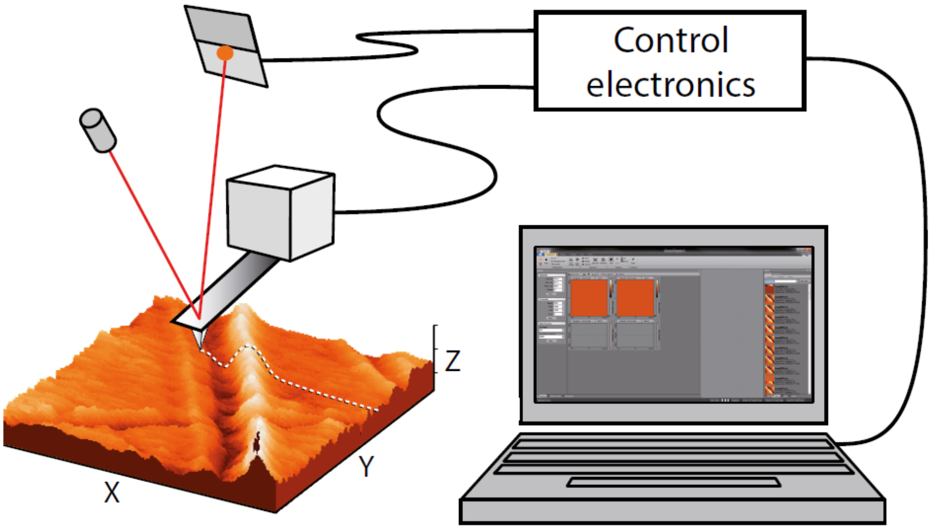

Figure 1.1: Schematic representation of the AFM set-up. In this configuration the actuator is attached to the probe stage and is moved over the stationary sample surface (source: FLEX AFM operating manual).

The beam deflection technique is the most common method to detect the cantilever deflection [25]. A laser beam from a laser diode is sent to and reflected off the back of the cantilever onto a position sensitive photodiode, which senses the change in light intensity caused by the cantilever deflection [26]. The purpose of the feedback loop is to maintain a predefined set-point, be it a force, amplitude or a frequency. For most operating modes a simple feedback controller (PI) is sufficient to fulfil this task with the exception of FM-AFM, where multiple controllers are required [5, 27]. AFM scanner actuators are made from piezoelectric material, which has the property that it expands and contracts proportionally to an applied voltage. Commonly, tube scanners are used in AFM systems, which can move in the X-, Y- and Z-directions using only a single tube piezo. There are two types of scanner configurations, one where the actuator is attached to the probe stage and is moved over the stationary sample surface, and the other where it is attached to the sample stage and moved below the stationary probe, see Fig. 1.1.

1.2. Amplitude Modulation Atomic Force Microscopy

In AM-AFM, sample surfaces are scanned with a vibrating cantilever that is driven at or near its first resonance frequency, and with every oscillation, the tip briefly touches the sample. Initially, when far from the sample, the oscillation amplitude is (almost) equivalent to the free vibration amplitude. When the sample is approached by the user, the amplitude reduces as a result of tip-sample interaction. It continues to reduce until a user defined value is reached. This designated value is the amplitude set-point, which is often defined as a percentage of the free vibration amplitude. While the surface is scanned, the oscillation amplitude tends to change as a result of the tip interacting with a sample containing topographic features and/or different materials. A feedback loop monitors the amplitude and keeps it constant by modifying the distance between the sample and the cantilever base.

As the tip completes an oscillation cycle in AM-AFM, it experiences two force regimes. When relatively far from the sample surface, the tip undergoes long-range attractive forces. When the tip starts touching the sample, the tip experiences short-range repulsive forces. The highest repulsive force is found when the tip is in contact with the sample and furthest away from its equilibrium position. The interaction between tip and sample is observed in the change of the resonance frequency of the cantilever, attractive forces cause a decrease whereas repulsive forces an increase. In AM-AFM, the cantilever is excited near or at its first resonance frequency. Attractive interaction will result into a shift of the resonance curve to lower frequencies whereas with repulsive interaction it shifts to higher frequencies. Consequently, the drive amplitude changes. This behaviour is demonstrated in Fig. 1.2.

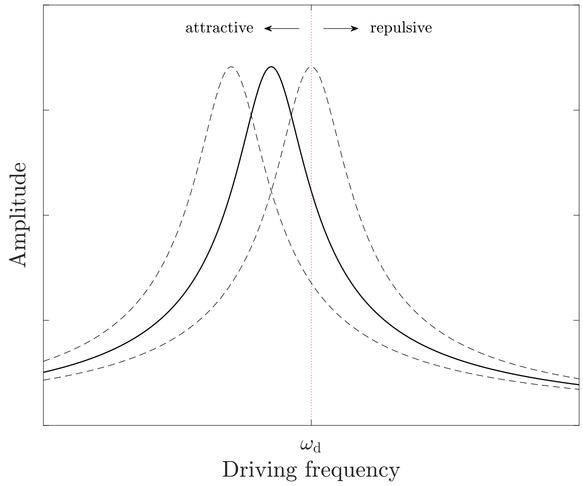

Figure 1.2: Frequency response, simulated for a Single Degree Of Freedom (SDOF) harmonic oscillator when it is excited just above resonance (solid line) and under influence of attractive and repulsive forces (dashed lines). Without any external force the system is excited just above resonance (dotted line) at ω_d.

Both the attractive and repulsive forces are highly nonlinear and therefore induce nonlinear behaviour in the AFM cantilever vibration. The presence of these forces emerges an intriguing property of AM-AFM, the coexistence of two stable oscillation states, at a single frequency the cantilever can vibrate with two distinct amplitudes [13, 21, 28–30]. The strength of the nonlinear interaction depends on sample, cantilever and tip properties [13, 31]. Bi-stable behaviour in the amplitude of the cantilever can also be inspected in the frequency response. Its resonance frequency becomes a function of the excitation amplitude when subjected to the nonlinear forces [13, 28, 32–37]. Another consequence of the nonlinear force potential is the introduction of higher harmonics in the frequency spectrum of the cantilever, which are integer multiples of the driving frequency. A frequency spectrum of an AFM cantilever containing higher harmonics marks the presence of nonlinear interaction forces [35, 38–41]. These nonlinear phenomena are directly related to the geometry and size of the nanoscale tip, since it is the only part of the cantilever interacting with the sample. Knowledge of the tip condition is therefore crucial for performing measurements with high accuracy.

1.3. Previous Research on Tip Identification

1.3.1. Tip Estimation with Electron Microscopy

Several methods to characterize the tip shape have been proposed. A common procedure is using a Scanning Electron Microscope (SEM) to asses the tip quality [42]. With SEM, high-precision images with nano-meter resolution can be obtained. An alternative is to use a high resolution transmission electron microscope (HR-TEM). It has been shown that with HR-TEM the crystalline structure of a silicon tip can be quantified [43]. However, there are some limitations and complications paired with these methods. The main drawback of both SEM and HR-TEM is that they are not able to quantify the tip in-situ, the tip wear can only be inspected at the end of a measurement. Recently though, *in-situ* characterization of the tip wear has been performed using an AFM implemented within an HR-TEM [44]. Another limitation of electron microscopy is that only semi-quantitative determination of the tip shape is possible, as the method only provides a two-dimensional profile of the tip. It should be noted that by using electron microscopy methods for tip characterization, there is always the risk of carbon deposition during observation [45].

1.3.2. 'Blind Tip Reconstruction'

An alternative method to determine the tip shape, is the Blind Tip Reconstruction (BTR) [46, 47]. This method exploits the fact that a topographic image obtained with AFM is a convolution of the tip geometry and the features on the sample surface. The first step of BTR is imaging a sample with calibrated small and sharp features. With post-processing of the topographic image a 3D approximation of the tip shape can be reconstructed. BTR has been experimentally validated by comparing it to results obtained by SEM and HR-TEM [43, 48, 49]. One of the disadvantages of BTR is that it can only reconstruct the tip geometry over a region that is a few nanometers from the tip apex. In practice, a combination of BTR and HR-TEM imaging can be used. BTR can determine the portion of the tip that is directly interacting with the sample and the data acquired by HR-TEM is used to identify the tip apex [43]. However, because for each measurement an additional approach and scan of the calibrated sample needs to be performed, BTR has an increased risk of damaging the tip.

1.3.3. Exploiting the Tip-Sample Interaction

The tip geometry can be extracted from topographic data, but the interaction forces are affected by the size of the tip as well, especially the long-range attractive forces show a strong dependency. Using static mode force-spectroscopy, the nonlinear forces have been analyzed in a fitting procedure to estimate the value of the tip radius [50]. Dynamic mode AFM is potentially another non-destructive way of estimating the tip radius during AFM measurements. Analysis of the tip-sample interaction can be performed by the acquisition of vibration amplitude-distance curves, the use of amplitude-frequency response curves, or by extracting the Fourier spectrum of the driving signal.

Exploring the first option, a method has been developed to identify the tip sharpness by inspecting the transitions from attractive to repulsive force regimes [51]. The tip radius is linked with a power law to the so called critical amplitude, which is the amplitude where bi-stability of two oscillation states is present. The method is found to be quite robust, showing accurate results for a range of different cantilever-sample combinations. The disadvantage in this method is that the magnitude of the power law needs to be identified empirically. For each cantilever-sample combination a separate power law has to be found. Other studies have exploited the nonlinearities for parametric identification in dynamic AFM. So has it been shown that a harmonic balance based identification method can be applied to extract material constants from the nonlinear vibration spectrum of the cantilever [52].

1.4. Research Question & Strategy

Recent advances of AFM are related to the development of techniques based on spectral analysis. Several studies related to AFM have been making use of higher modes, harmonics and nonlinear frequency response curves. Dynamic AFM holds a possible way of estimating the tip in-situ whilst minimizing further tip damage in the process. Based on this, the research question of the project is:

> *How can nonlinear dynamics be used to estimate the tip condition in AFM?*

In order to provide an answer to this question, first the theory regarding the complicated cantilever motion when it interacts with a sample surface is investigated. Based on the insight gained, a methodology to identify the tip radius is developed. In order to validate the method, experimental results, which are acquired with novel systematic procedures are compared to numerical simulations.

2

Mechanics of the Tip-Sample Interaction

Due to the nonlinear nature and complexity of the tip-sample interaction forces, it is difficult to predict the cantilever motion. A variety of forces make up the AFM force potential and a lot of research has been spent on the interpretation and approximation of these forces. Knowledge about the tip-sample mechanics models is essential for accurate modelling and prediction of the cantilever motion and tip estimation. In the following sections, the various components of the AFM force potential will be explored. Furthermore the different theories that describe the tip-sample interaction are explored. Because there is no singular model that can describe all types of interaction, a suitable model has to be chosen.

2.1. The Tip-Sample Interaction Potential

When an AFM cantilever is brought in proximity of a surface, the tip-sample interaction forces cause a change in its vibration amplitude. Understanding the tip-sample interaction is essential for a study on tip identification, since the forces are highly dependent on the tip size. The interaction forces are divided into long-range attractive and short-range repulsive forces [53, 54]. In the tapping mode, the tip undergoes both these force regimes. This can be further inspected by closer inspection of the exemplary tip-sample force potential plotted in Fig. 2.1. The tapping mode oscillation cycle corresponds to a path from A to C and back along the force potential. Other operating modes will follow different paths, such as the noncontact mode, where a single oscillation follows the force potential from A to B and back.

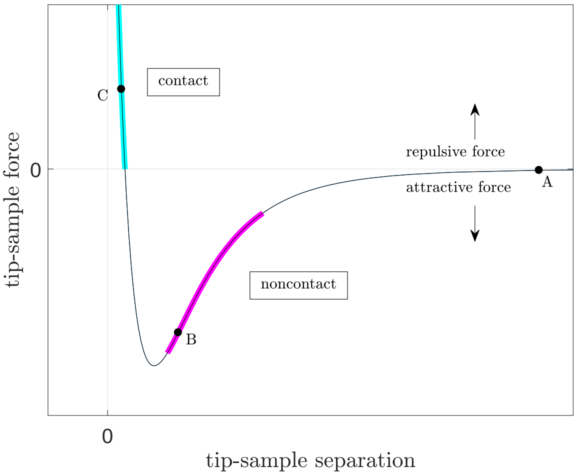

Figure 2.1: The AFM force potential, which the force-distance relation between tip and sample, the contact (blue) and noncontact (magenta) regions are indicated. A is a point on the force potential where the cantilever is far away from the sample and barely affected by the attractive forces. B is a point closer to the sample, where the cantilever experiences an attractive force. C is a point where there is contact between tip and sample and the net force on the cantilever is repulsive.

2.2. The Lennard-Jones Potential

In order to formulate the long-range attractive forces, it is important to first describe the model that is used to specify the interaction between two atoms or molecules, the Lennard-Jones potential. The Lennard-Jones potential between two neutral atoms or molecules is

$$U_{\mathrm{LJ}}(r) = 4U_0\left(\left(\frac{\sigma}{r}\right)^{12} - \left(\frac{\sigma}{r}\right)^{6}\right), \tag{2.1}$$

where U_0 is the potential depth, r the distance between the two particles and σ is the finite distance at which the potential is zero ($U_0(r=\sigma)=0$), adapted from [55]. If two atoms are brought in very close proximity to each other, due to overlapping electron orbitals there is an extremely strong repulsive force between the two of them. This is called Pauli exclusion and is described by the r^{-12} term. The r^{-6} term expresses the long-range attractive dispersion forces or Van der Waals forces. The attractive term has a clear physical justification whereas the repulsive term is empirically found. Differentiation of the Lennard-Jones potential with respect to the separation distance r gives the expression for the force F_{LJ} between two neutral atoms or molecules as

$$F_{\mathrm{LJ}}(r) = -\frac{\partial U_{\mathrm{LJ}}}{\partial r}. \tag{2.2}$$

2.3. Long-Range Interaction Forces

There are three main contributors to the long-range interaction forces, the Keesom, Debye and London force, which are related to mutual attraction between dipoles and their temporary formation. The Keesom force describes the interaction between permanent dipoles. The interaction between permanent and induced dipoles is known as the Debye force and the London force covers the interaction between induced dipoles. Their sum is also known as the van der Waals force. Their potential U is related to the separation distance as r^{-6}. Addition of the Keesom, Debye and London potential gives an expression for the van der Waals potential as

$$U_{\mathrm{vdW}}(r) = U_{\mathrm{K}}(r) + U_{\mathrm{D}}(r) + U_{\mathrm{L}}(r) = \left[C_{\mathrm{K}} + C_{\mathrm{D}} + C_{\mathrm{L}}\right]\frac{1}{r^6} = -\frac{C_{\mathrm{vdW}}}{r^6}. \tag{2.3}$$

In order to model the interactions between tip and sample, it is necessary to consider continuum bodies. Assuming that the net interaction force is equal to the sum of its interactions with all molecules in the body, the Van der Waals energies between bodies can be calculated by integration using Derjaguin's approximation [56]. Typically in AFM, the tip-sample geometry is modelled as a (hemi-)sphere with a radius R and a flat surface [57]. If the tip is considered (hemi-)spherical, the van der Waals forces are equal to

$$F_{\mathrm{vdW}}(d) = -\frac{HR}{6d^2}. \tag{2.4}$$

Here H, R and d are the Hamaker constant, the tip radius and the instantaneous tip-sample separation, respectively. Hamaker constant can be defined for a van der Waals body-body interaction as

$$H = \pi^2 C_{\mathrm{vdW}}\rho_1\rho_2, \tag{2.5}$$

where ρ_1 and ρ_2 are number densities of the two different materials. The tip-sample distance d is expressed as $d = z_{\mathrm{c}} + z$ where z_{c} is the separation between the cantilever base and the sample surface and z the cantilever deflection in the negative Z-direction with respect to its rest position, as shown in Fig. 2.2.

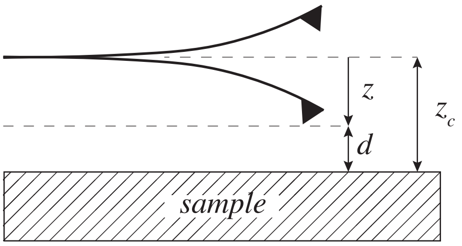

Figure 2.2: Schematic of the AFM and the sample surface. The rest position of the cantilever acts as reference for its deflection z. This figure is adopted from the publication in Applied Physics Letters [1].

Besides elementary tip shape approximations ((hemi-)spherical, flat-circular, conical and paraboloid [23, 58, 59]) more sophisticated configurations have been introduced [50]. For the three common tip-sample geometries the van der Waals forces are given in Table 2.1. A comparison between the geometries of Table 2.1 is made in Fig. 2.3. For a flat-circular tip the separation distance, where the attractive force rises rapidly, is larger compared to the (hemi-)sphere or cone. The conical and (hemi-)spherical tip shape show a similar force-distance relation. In Fig. 2.4, the force-distance relation between a (hemi-)spherical tip versus a flat sample is calculated for a range of values of R. The force is the most sensitive to the tip size when R is relatively small ($R = [10, 50]\,\text{nm}$). A small change in tip size within these boundaries has a significant effect on the magnitude of the van der Waals force.

Table 2.1: Van der Waals interaction force derived for common tip-sample geometries, where R is the sphere radius, r is the radius of the flat-circular area and θ is the cone angle. Adapted from [4].

Geometry	van der Waals Force
two flat surfaces	$F = -\dfrac{H}{6\pi d^3}$ per unit area
sphere - flat surface	$F = -\dfrac{HR}{6d^2}$
flat-circular - flat surface	$F = -\dfrac{Hr^2}{6d^3}$
cone - flat surface	$F = -\dfrac{H\tan^2\theta}{6d}$

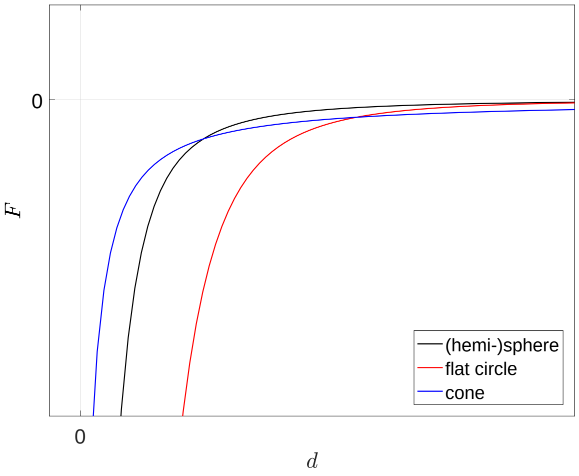

Figure 2.3: Plot of the force-distance relation for different tip geometries, visualizing the difference in the van der Waals forces between a (hemi-)spherical ($R = 10\,\text{nm}$), flat-circular ($r = 10\,\text{nm}$) and conical tip ($\theta = 20°$). Cantilever and material properties are kept constant throughout the simulations.

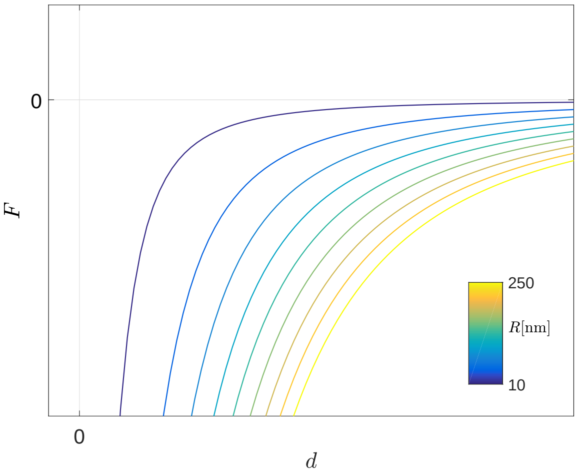

Figure 2.4: A series of force-distance curves for a (hemi-)spherical tip shape, for increasing values of the tip radius R.

It has been shown that the (hemi-)sphere is a good approximation for the tip geometry [57, 60]. Therefore, in the remaining parts of this work the tip geometry will be considered as (hemi-)spherical, unless stated otherwise. The van der Waals forces between tip and sample are assumed to be equal to Eq. (2.4).

2.4. Short-Range Repulsive Forces

By close inspection of the force potential displayed in Fig. 2.1, one can notice that in very close proximity to the sample the van der Waals forces are overruled by strong forces in the repulsive direction. These are known as short-range repulsive forces and are the result of adhesion, cohesion and surface tension phenomena. Multiple models are developed to describe the contact mechanics, such as the JKR (after Johnson, Kendall and Roberts) and the DMT (after Derjaguin, Muller and Toporov) model.

2.4.1. The Hertz Model

These models find their origin in the Hertz theory [15]. When the AFM tip indents the sample surface it creates a contact area, which can be modelled as a sphere with radius R indenting to an elastic surface with an indentation depth. With the Hertzian contact model we find for the applied force F related to the tip-sample separation d is

$$F_{\text{Hertz}}(d) = \begin{cases} 0, & d > 0 \\ \frac{4}{3} E^* \sqrt{R} (-d)^{\frac{3}{2}}, & d \leq 0, \end{cases} \tag{2.6}$$

where E^* is the effective Young's modulus calculated from E_{tip}, E_{sample} and the Poisson's ratios ν_{tip}, ν_{sample} associated with the tip and sample as

$$\frac{1}{E^*} = \frac{1 - \nu_{\text{tip}}^2}{E_{\text{tip}}} + \frac{1 - \nu_{\text{sample}}^2}{E_{\text{sample}}}, \tag{2.7}$$

adapted from [15, 55].

2.4.2. The DMT Model

The DMT model incorporates the fact that atoms interact with each other, even when they are not in contact [17, 55]. If the tip-sample separation exceeds the intermolecular distance, i.e. $d > a_0$, the tip only undergoes attractive van der Waals forces. If $d \leq a_0$, the net force on the tip is repulsive. The DMT force-distance relation is equal to

$$F_{\text{DMT}}(d) = \begin{cases} -\frac{HR}{6d^2}, & d > a_0 \\ -\frac{HR}{6a_0^2} + \frac{4}{3} E^* \sqrt{R} (a_0 - d)^{\frac{3}{2}}, & d \leq a_0. \end{cases} \tag{2.8}$$

2.4.3. The JKR Model

The JKR model incorporates the effect of adhesion in the Hertzian contact [16, 55]. The adhesive contact is formulated using a balance between the stored elastic energy and the loss in surface energy. The JKR model only considers the effect of adhesion and contact pressure inside the contact area. In addition, it describes hysteresis between the approach and retract operation. In the approach phase there is no interaction between tip and sample until they touch. Upon impact, there is a large attractive force present. As the indentation depth increases, the behaviour is identical to the Hertz and the DMT model. In the retract phase the jump from contact does not occur at $d = 0$ but at a critical distance $d = d_{\text{crit}}$, due to the work of adhesion. The JKR force-distance relation is equal to

$$F_{\text{JKR}}(d) = \begin{cases} 0, & \text{no contact} \\ \frac{4E^* a^3}{3R} - 4\sqrt{\frac{F_{\text{ad}} E^* a^3}{3\pi R}}, & \text{contact,} \end{cases} \tag{2.9}$$

where a is the radius of the contact area and F_{ad} the adhesion force, which is equal to

$$F_{\text{ad}} = \frac{9}{8} \frac{HR}{6a_0^2}. \tag{2.10}$$

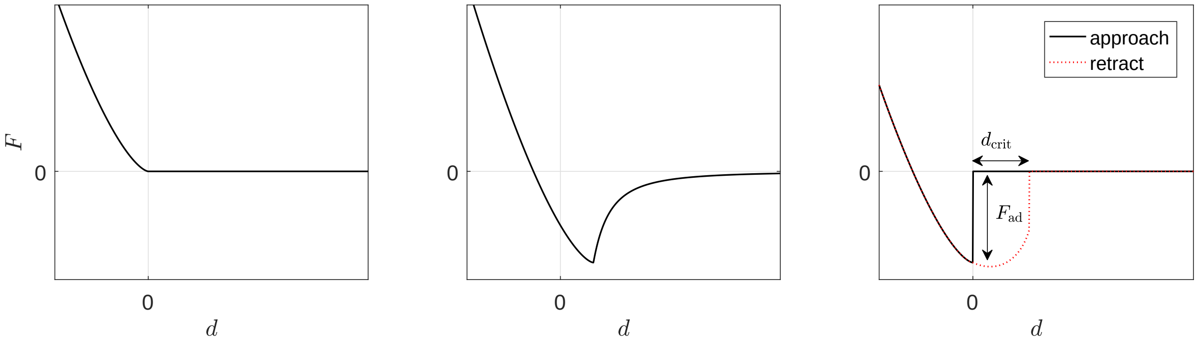

Figure 2.5: Force-distance relations for the different contact models. LEFT: Hertzian contact, describing repulsive interaction at zero separation. MIDDLE: DMT model, where a transition from attractive to repulsive interaction occurs at $d = a_0$. RIGHT: JKR model, where the effect of adhesion is incorporated. Hysteresis is observed between the approach and retract phase.

2.5. Electrostatic & Capillary Forces

Often unwanted but inevitably present forces in AFM are the electrostatic and capillary forces. On hydrophilic surfaces a thin water layer is often formed, especially in ambient conditions. If the tip and sample surface are in close proximity, a liquid bridge may be formed between tip and sample, which introduces an attractive capillary force [61, 62], as shown in figure 2.6. This effect can be minimized by controlling the relative humidity or performing experiments in vacuum. Trapped electrostatic charge in dielectric surfaces could imply the increase of long-range interaction forces. This especially holds for experiments where an external electric field is applied between tip and sample. Capillary and electrostatic forces can play an important part in experiments [41]. In order to conduct accurate experimental measurements the consideration of these forces is of vital importance.

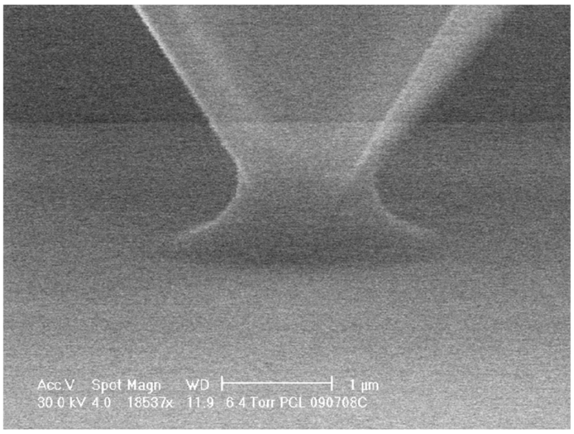

Figure 2.6: Water capillary bridge that is formed between tip and sample, observed in an SEM. The water bridge was obtained by drastically increasing the relative humidity (RH > 98 %). Adopted from [2].

2.6. Interaction Model Selection

To date, a universal contact model has not been developed, hence the previously mentioned models are suited for different types of contact. According to the elasticity parameter, which is proportional to the ratio between adhesion and elasticity, the different models are categorized [63]. It has been shown that the general solutions for 'stiff' contact, reduce to the Hertz or the DMT model. The DMT model is especially suitable for describing stiff contacts with low adhesion forces and small tip radii. The JKR model is suited for contacts characterized by high adhesion, low stiffness and large tip radii, or in other words, 'soft' contact. In the remaining of this work the DMT contact model is used because experiments will be performed on relatively hard samples, and the relative humidity will be controlled. The total interaction force between tip and sample is chosen to be equal to Eq. (2.8) in the remaining parts of this work.

3

Nonlinear Cantilever Dynamics in AM-AFM

In AM-AFM the cantilever is driven to oscillate at or near its resonance frequency. The cantilever signal is therefore expressed in vibration amplitude and phase. The interaction between tip and sample can be detected by observing the change in resonance frequency of the cantilever. If excited above its first resonance frequency, attractive interaction will result in a higher drive amplitude of the cantilever and repulsive interaction in a lower one as previously shown in Fig. 1.2. Due to the nonlinear nature of the tip-sample interaction, the cantilever can vibrate in seemingly unpredictable ways. Knowledge about the associated nonlinear dynamics allows one to model its motion, which can serve as a useful tool for tip characterization. The numerical simulations in this report are obtained using the bifurcation analysis package AUTO [64].

3.1. Equation of Motion

A thorough understanding of AM-AFM is found in deriving the Equation Of Motion (EOM) of the cantilever-tip ensemble interacting with the sample surface. The most thorough approach involves solving the EOM of a cantilever beam. Under symmetry conditions, one would allow to approximate the cantilever beam by a one-dimensional object, then

$$EI\frac{\partial^4 w(x,t)}{\partial x^4} + \mu\frac{\partial^2 w(x,t)}{\partial t^2} = F(x,t). \tag{3.1}$$

Here $w(x,t)$ describes the vertical displacement of the cantilever beam, E, I and μ are Young's modulus, mass moment of inertia and mass per unit length of the cantilever, respectively. $F(x,t)$ is the sum of all the forces per unit length acting on the tip. The implicit assumption made here is that the tip itself is considered a massless object. Several methods have been developed to solve this particular equation [65–67]. From a dynamics point of view, the cantilever-tip ensemble is often modelled as a point-mass spring system [28, 33, 68–72]. The tip motion is then governed by a nonlinear, second order differential equation

$$\frac{\partial^2 z}{\partial t^2} + \frac{m\omega_\mathrm{n}}{Q}\frac{\partial z}{\partial t} + k_\mathrm{c} z = F_0\cos(\Omega t) + F_\mathrm{ts}, \tag{3.2}$$

where z, Q, ω_n and k_c are the deflection, quality factor, angular resonance frequency and the stiffness of the cantilever, respectively. F_0 and Ω are the amplitude and angular frequency of the excitation force. F_ts corresponds to the total tip-sample interaction force which is equal to Eq. (2.8). For further analysis it is convenient to consider the non-dimensional form of Eq. (3.2):

$$\frac{\partial^2 \hat{z}}{\partial \tau^2} + \hat{c}\frac{\partial \hat{z}}{\partial \tau} + \hat{z} = \lambda\cos(\hat{\Omega}\tau) + \hat{F}_\mathrm{ts}. \tag{3.3}$$

According to the schematic representation of Fig. 2.2, the spatial parameter is normalized to z_c. Time is made dimensionless by considering $\tau = \omega_\mathrm{n} t$. The non-dimensional deflection and dissipation coefficient are governed by $\hat{z} = \frac{z}{z_\mathrm{c}}$ and $\hat{c} = \frac{1}{Q}$, whereas $\lambda = \frac{F_0}{z_\mathrm{c} k_\mathrm{c}}$ represents the sinusoidal excitation with frequency $\hat{\Omega} = \frac{\Omega}{\omega_\mathrm{n}}$.

The tip-sample interaction force is then governed by

$$\hat{F}_{\mathrm{ts}}(\hat{z}, z_{\mathrm{c}}) \begin{cases} -\dfrac{HR}{6z_{\mathrm{c}}^3 k_{\mathrm{c}}} \dfrac{1}{(1+\hat{z})^2}, & \hat{z} > \dfrac{a_0}{z_{\mathrm{c}}} - 1 \\ -\dfrac{HR}{6a_0^2 z_{\mathrm{c}} k_{\mathrm{c}}} + \dfrac{4E^* \sqrt{R}}{3 z_{\mathrm{c}} k_{\mathrm{c}}} \big(a_0 - z_{\mathrm{c}}(1+\hat{z})\big)^{\frac{3}{2}}, & \hat{z} \leq \dfrac{a_0}{z_{\mathrm{c}}} - 1. \end{cases} \tag{3.4}$$

More information regarding the derivation of the dimensionless EOM can be found in Appendix A.1.

3.2. Coexistence of Multiple Oscillation States

The participation of nonlinear attractive and repulsive tip-sample interactions result to an exciting characteristic of AM-AFM, the coexistence of two stable oscillation states [13, 21, 28–30]. In extreme cases, such as with very small tip-sample separation and very large oscillation amplitudes, more than two stable or even chaotic solutions can be found[73–76]. The representation of the amplitude as a function of the tip-sample separation gives an insight to the bi-stable behaviour. This representation is also known as an amplitude-distance (A-d) curve. In an experimental setting, A-d curves are obtained by measuring the cantilever amplitude while it is approached to and retracted from the sample.

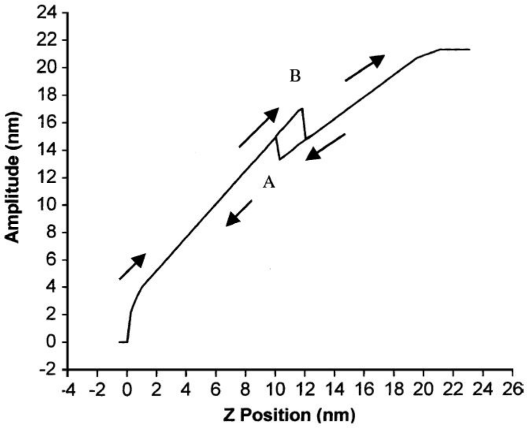

Figure 3.1: Experimental A-d curve (approach and retract phase) taken on a mica sample. Partial sections of the high and low amplitude branches are observed. A is the point in the approach phase where a transition from the low to the high amplitude branch occurs. B is the point in the retract phase were a transition from the high to the low amplitude branch takes place. Adopted from [3].

Fig. 3.1 shows both a simulated and experimentally obtained A-d curve. The simulation shows two solution branches for a range of different tip sample separations. In reality the tip cannot be in two distinct oscillation states at once, with as a result that the two branches cannot be experimentally measured simultaneously. In the experimental curve, discontinuities at A and B indicate a transition between the low and high amplitude solution. A hysteresis loop can be observed in the middle section of the A-d curve, which means there are two state transitions at different tip-surface separation distances. Typically, at large separations the tip oscillates in a state that coincides with the low amplitude solution, whereas with small separations the tip vibrates with high amplitude. The hysteresis between the up- and downward transition is repeatable for a given system, but the tip-sample distance at which a transition occurs may change. Since the equation of motion of the tip has a deterministic nature, the tip tends to remain in its original state or solution branch. A transition from one branch to another therefore requires a perturbation in the system. Because perturbations occur at random, one might observe amplitude curves with multiple state transitions [77].

The bi-stable behaviour in the amplitude of the cantilever can also be inspected in the frequency response. It is useful to extract the information near the first resonance frequency of the cantilever subjected to interaction forces. In principle, if an harmonic oscillator undergoes nonlinear interaction, it will result to bending of its resonance frequency peak. In AM-AFM, the nonlinear interaction forces have the same effect on the frequency response of the cantilever tip [32, 34–37]. In Fig. 3.2 this bending behaviour is demonstrated for three cases. The location of the variation of the nonlinear frequency shift for increasing values of the tip oscillation amplitude is referred to as a backbone curve. Attractive van der Waals forces cause a bending of the resonance peak to lower frequencies, called softening. If the tip is subjected to repulsive contact forces, the resonance peak bends to the right, which is called hardening. A combined attractive-repulsive potential results in initial softening, with a transition to hardening.

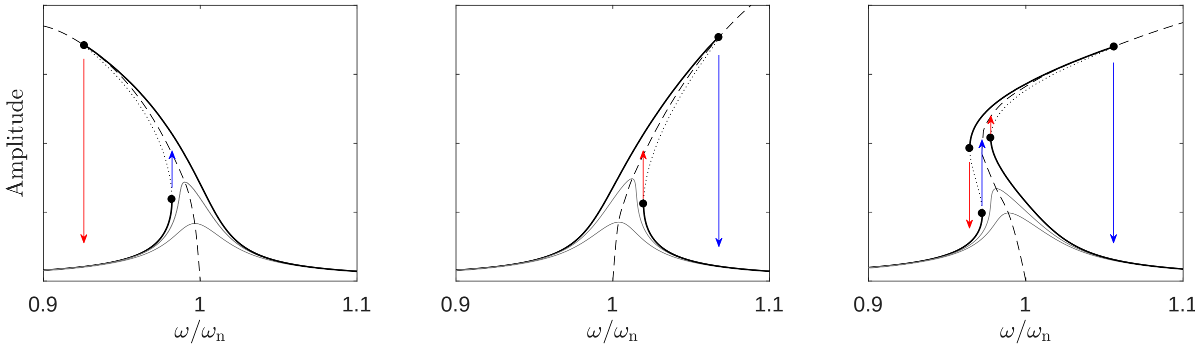

Figure 3.2: Numerical simulations of a nonlinear SDOF harmonic oscillator, demonstrating bi-stability and hysteresis in the frequency response when subjected to attractive and/or repulsive forces. The backbone curves are illustrative and not obtained with numerical simulations (black dashed line). LEFT: Exclusively attractive interaction. Experimentally, because an unstable solution (black dotted line) cannot be obtained, at the saddle-node point (black dot) a jump from one to the other stable branch takes place (arrow). For very small oscillations the resonance can be approximated by a linear oscillator. MIDDLE: Purely repulsive interaction, showing similar behaviour in the other direction. RIGHT: Result of an attractive-repulsive potential on the frequency response curve, showing both softening and hardening.

3.3. Higher Modes & Higher Harmonics

So far, the effect of the nonlinear phenomena on the cantilever vibration have been discussed on the basis of a SDOF model. The microcantilever, however, is a structure capable of multiple types of oscillation, such as bending or twisting [78, 79]. If these higher modes of vibration are added to the model, accuracy is improved. Higher order models are especially required if the cantilever is excited at multiple frequencies at once and are able to predict the spectrum of higher harmonics of the cantilever response [80].

When subjected to nonlinear forces in tapping mode, the cantilever motion generates frequency components above the driving frequency. Due to the periodic nature of the impact, the response is condensed in harmonics, which are frequencies at integer multiples of the driving frequency. A frequency spectrum of an AFM cantilever containing higher harmonics thus marks the presence of nonlinear interaction forces [35, 38–41]. An example of a frequency spectrum containing higher harmonics is shown in Fig. 3.3. Higher frequencies are sometimes deliberately introduced to sense the nonlinear interaction, which is often done in surface topography measurements. The sample is then tracked by the fundamental mode while a higher mode or harmonic oscillating with a smaller amplitude is used for mapping of the sample surface. Bimodal AFM is an example of this, where the cantilever is excited at two eigenmodes at once [81, 82]. Higher harmonic/modal imaging proves to be useful to monitor the imaging conditions in tapping mode and is often applied to increase the material contrast [83, 84]. Higher harmonic imaging experiments and more information about its working principle can be found in Appendix B.3.

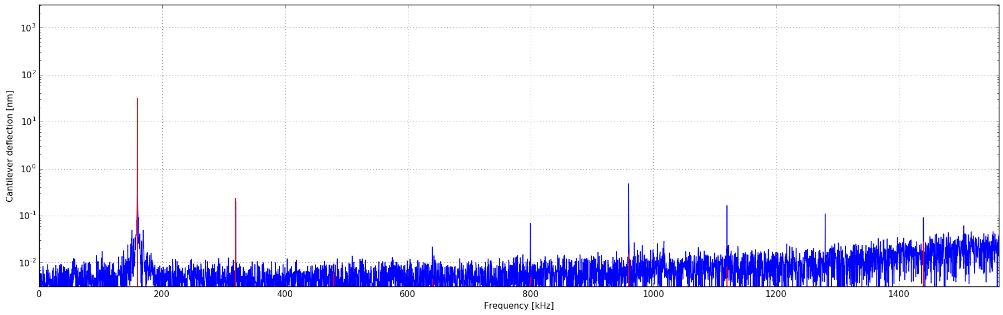

Figure 3.3: Experimental frequency spectrum of an AFM cantilever during tapping mode operation. The highest red line signifies the location of the driving frequency and the other red lines mark the integer multiples, i.e. harmonics.

4

Experimental Methodology

4.1. Experimental Setup

In order to perform an identification study on the tip radius, experiments need to be performed, for which an experimental AFM set-up is required. The set-up consists of a commercially available AFM (Nanosurf FLEX operated with the C3000 controller) and an external multi-frequency lock-in amplifier (Intermodulation Products AB) directly connected to the AFM unit.

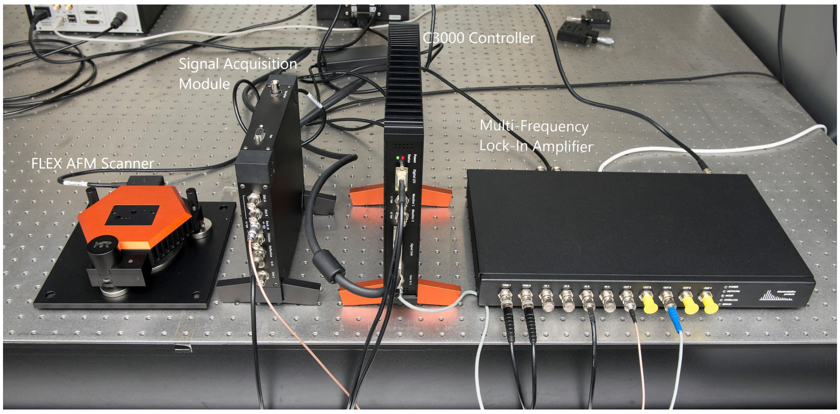

Figure 4.1: Overview of the complete experimental set-up placed on a vibration isolation platform. From left to right: the FLEX AFM scanner, the signal acquisition module or breakout box, the C3000 controller and the multi-frequency lock-in amplifier.

4.1.1. The AFM Scanner and Controller

The FLEX AFM is a versatile system which can perform imaging and spectroscopy in both the static mode and dynamic mode. Due to its smart design it allows for fast changing of cantilever and/or sample. The piezo-electric scanner is attached to the probe stage and is moved over the stationary sample stage. The bandwidth of the photodetector is 4 MHz.

4.1.2. The Multi-Frequency Lock-In Amplifier

The multi-frequency lock-in amplifier (MLA) is able to calculate in real-time, the response from the system input at 42 user-defined frequencies. It has a significantly higher bandwidth than the photodetector, making it ideal for high frequency analysis in AFM. With an added software suite, its capabilities increase further. In Fig. 4.2 the connections between AFM, controller, signal acquisition module and MLA are visualised. Inputs to the MLA are the photodetector signal, end-of-line (EOL) and end-of-file (EOF) triggers. The MLA has a built-in controller, with the same working principle as the AFM controller. With access on the external drive, frequency sweeps can be performed to find the resonance frequency. Additional cantilever calibration based on the non-invasive thermal noise method can be carried out. The amplitude and phase of the locked-in frequencies can be visualized and synchronized with the host AFM, allowing for harmonic imaging.

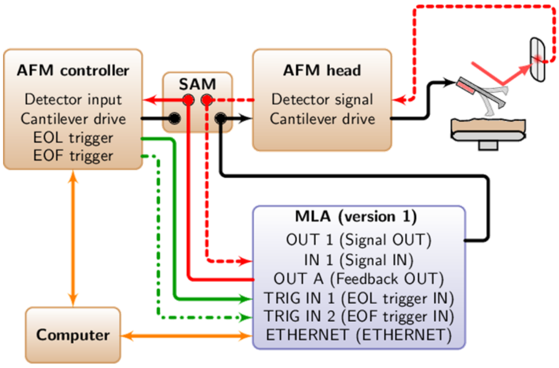

Figure 4.2: Overview of the connections between the AFM, controller, signal acquisition module (SAM) and MLA. The red line marks the photodetector signal, the green lines represent the EOL and EOF triggers and the black line the cantilever drive signal (source: `http://www.intermodulation-products.com/`).

4.1.3. Experimental Environment, Conditions & Considerations

Tthe cantilever probes used in the experiments are commercially available (type NCLR and FMR, NanoWorldAG). A complete specification of the used cantilevers are available in Appendix C.2. The manufacturer guarantees a nominal tip radius of $R < 12\,\text{nm}$ for both cantilever types. The experiments were performed at $T \approx 20\,°\text{C}$. For each experiment the laser was positioned near the tip end of the cantilever, for the reason that the theoretical considered amplitude is at the tip's location. In order to minimize the effect of the capillary forces, during quantitative experiments the relative humidity of the experimental environment was controlled (RH < 10 %). This was achieved by placing the AFM scanner in an enclosed environment with dry silica. In order to reduce external vibrations the set-up is placed on a vibration isolation platform.

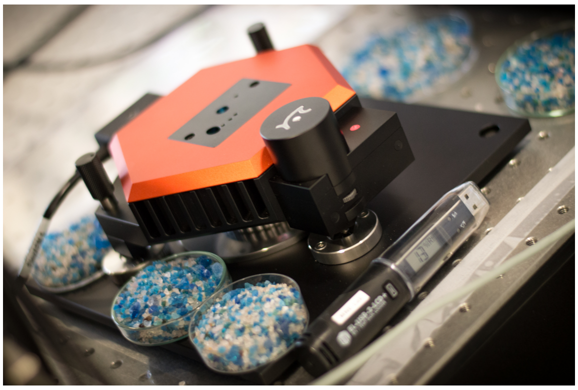

Figure 4.3: The AFM scanner surrounded by Petri dishes filled with dry silica. In this picture the chamber was removed, hence the humidity is immediately increased to 13 %, indicated by the sensor.

4.2. Probing the Attractive Forces

In order to find a method for tip identification, it is important to consider in which force regime the cantilever vibration shall be measured. In regular tapping mode, the tip moves through both attractive and repulsive regions of the tip-sample potential. The magnitude of repulsive interaction shows dependency on the local sample elasticity. Recalling Eq. (2.8), the repulsive forces show a proportionality to $\sqrt{R}$, whereas the attractive forces are directly proportional to R. Therefore, it would be beneficial to measure the cantilever vibration in the attractive regime, maximizing the influence of R on the nonlinear response. Note that the van der Waals forces are generally more delicate compared to the strong repulsive forces, with the consequence that the nonlinearities are smaller in magnitude and therefore more difficult to extract. It is possible to achieve non-contact operation in AM-AFM, but a low amplitude set-point needs to be maintained, which might cause instability.

4.2.1. Attractive Forces & Higher Harmonics

Previous studies have shown that higher harmonics are being generated due to tip-sample interaction [38, 85]. Another study has shown the presence of higher harmonics in the attractive regime should be directly correlated to the van der Waals forces [41]. The results of this study suggest that systematic measurement of higher harmonics in the attractive regime can lead to highly accurate methods of identification. The experimental set-up is suitable for extracting higher harmonics, since the MLA contains 42 individual lock-in channels. With nonlinear system identification techniques, such as harmonic balance, the higher harmonic signals can be used for tip quantification. Harmonic balance is a method to find the steady state solution of free and forced nonlinear systems by assuming the response of the system is periodic and can be expressed as a series of harmonics. The solution of Eq. (3.3) can be approximated with a truncated Fourier series as

$$\hat{z} \approx \hat{z}_N = \hat{z}_0 + \sum_{k=1}^{N} a_n \cos kt + b_n \sin kt, \tag{4.1}$$

where N is the order of truncation and $\hat{z}_N$ is the truncated Fourier Series representation of $\hat{z}$. The higher the order of truncation, the better the approximation. For this reason, the aim is to find an experimental frequency spectrum of the cantilever with a collection of higher harmonics excited above noise level.

Fig. 4.4 shows the experimental Fast Fourier Transform (FFT) from the time signal at different amplitude reduction set-points. For this particular experiment the FMR type cantilever and a mica sample are used. For a dynamic mode type, the FMR cantilever has a relatively low stiffness, therewith increasing its sensitivity to the nonlinearities. The set-points are expressed as $\frac{z_{\mathrm{red}}}{z_{\mathrm{free}}} \times 100\,\%$, where z_{red} is the reduced amplitude due to tip-sample interaction and z_{free} the free vibration amplitude. At $[75\,\%, 85\,\%]$, there is little to no higher harmonic excitation, except for $2\omega_{\mathrm{d}}$. In the interval $[55\,\%, 65\,\%]$, more harmonics are excited. Even a small peak between $6\omega_{\mathrm{d}}$ and $7\omega_{\mathrm{d}}$ can be observed, indicating the second vibration mode. Within $[35\,\%, 55\,\%]$, there is less generation of higher harmonics. Note that the amplitude of $2\omega_{\mathrm{d}}$ reduces in these set-points, where it remained proportional to the driving frequency for $[55\,\%, 85\,\%]$. An additional experiment was carried out and suggests the excitation of $2\omega_{\mathrm{d}}$ is the result of other nonlinear effects, for more information see Appendix B.2. As a result of the strong repulsive interaction, at set-points $\leq 65\,\%$ multiple harmonics are being generated. This suggests that for set-points $\geq 75\,\%$ there is attractive interaction. As mentioned earlier, the attractive forces are generally more gentle than the repulsive forces, hence the reason that hardly any higher harmonic signals seem to rise above the noise floor.

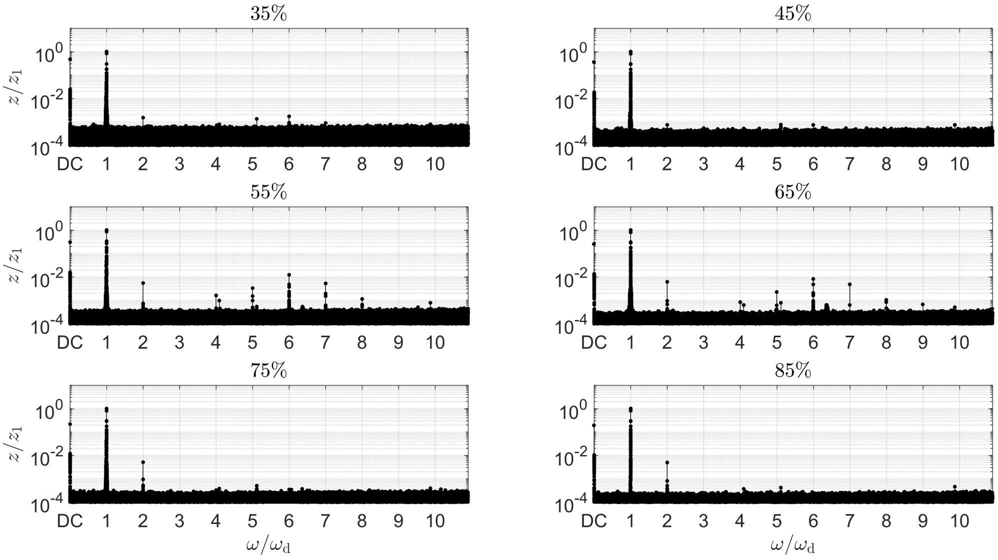

Figure 4.4: Experimental frequency spectra of an FMR cantilever interacting with a mica sample at different amplitude reduction set-points. The frequency and amplitude are normalized with respect to the driving frequency $\omega_{\mathrm{d}} = 71.7\,\mathrm{kHz}$.

To get a better view at which point the harmonics are being generated a different experiment has been performed. An A-d measurement is executed while the MLA locks in to the higher harmonics. The goal of this measurement is to observe the behaviour of higher harmonics at the point of transition between the attractive and repulsive regime. The following experiment was performed with the NCLR cantilever, which has a higher stiffness and resonance frequency compared to the FMR type. Fig. 4.5 shows the A-d curve for the driving frequency and 9 higher harmonics. Some harmonics such as $3\omega_\mathrm{d}$ and $4\omega_\mathrm{d}$ hardly rise above noise, whereas others are clearly being excited. On the left side of the red line, which marks the attractive regime, other than ω_d only $2\omega_\mathrm{d}$ has a significant magnitude. At the point of transition, $2\omega_\mathrm{d}$ decreases but $6\omega_\mathrm{d}$, $7\omega_\mathrm{d}$ and $9\omega_\mathrm{d}$ increase in a similar trend.

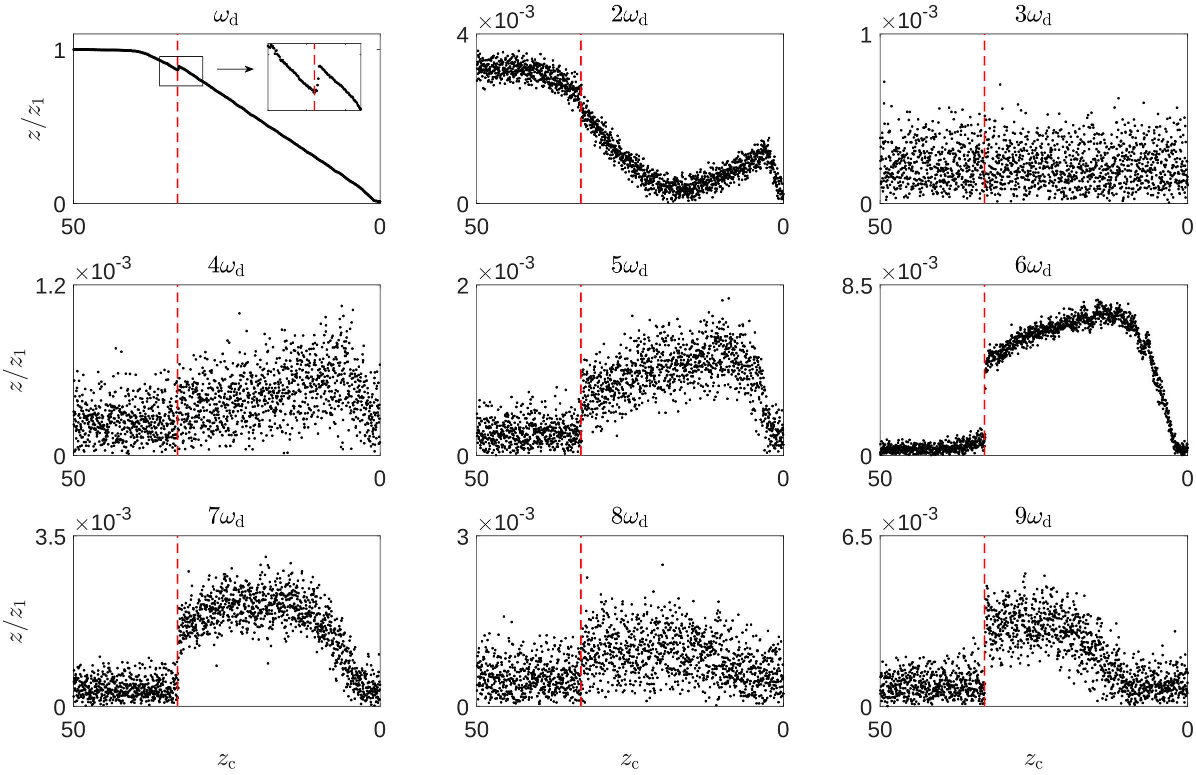

Figure 4.5: Experimental dynamic approach measurement where the driving frequency and several higher harmonics are tracked simultaneously, starting from $z_\mathrm{c} \approx 50\,\mathrm{nm}$ until the sample is reached ($z_\mathrm{c} \approx 0\,\mathrm{nm}$). The dashed line marks the transition from attractive to repulsive regime. The signals are normalized with respect to the free vibration amplitude of the drive frequency $\omega_\mathrm{d} = 163.7\,\mathrm{kHz}$.

Even though both measurements were performed with different cantilevers, their results show similarities. In the attractive regime there is little to no generation of higher harmonics, except for $2\omega_\mathrm{d}$. At the point of transition there is a sudden excitation of $5\omega_\mathrm{d}$, $6\omega_\mathrm{d}$ and $7\omega_\mathrm{d}$, and they decrease as the cantilever moves further into the repulsive regime. The conclusion drawn from both experiments is that the magnitude of the higher harmonics in the attractive regime are not high enough to be used for nonlinear parametric identification. On the other hand, in the repulsive regime, the harmonics are high above noise. It is reasonable to assume that nonlinear harmonic based parametric identification in the repulsive regime could be carried out successfully.

4.2.2. Influence of Attractive Forces on the Frequency Response

The possibility of extracting higher harmonics was explored first, because it is especially suited for numerical identification techniques. Experiments have pointed out that the higher harmonic signals are not strong enough to be exploited. The peak in the cantilever's oscillation cycle should approach the maximum attractive force, close to point B in Fig. 2.1, in order to obtain the highest possible nonlinearity rising solely from the van der Waals forces. A disadvantage regarding the inspection of higher harmonics is that it's difficult to specify the proximity to this maximum attractive force. A method in which the measurement can indicate the covered force potential is therefore preferred.

The external drive access of the MLA allows for frequency sweeps to be performed in a controlled way. The driving voltage, frequency range and interval can be specified with high precision. Additionally, the frequency sweeps can be executed from low to high (forward sweep), or from high to low frequency (backward sweep). With the combination of both forward and backward sweep, all stable solutions for a softening, hardening or combined frequency response curve can be obtained. This is demonstrated for a combined case in Fig.4.6.

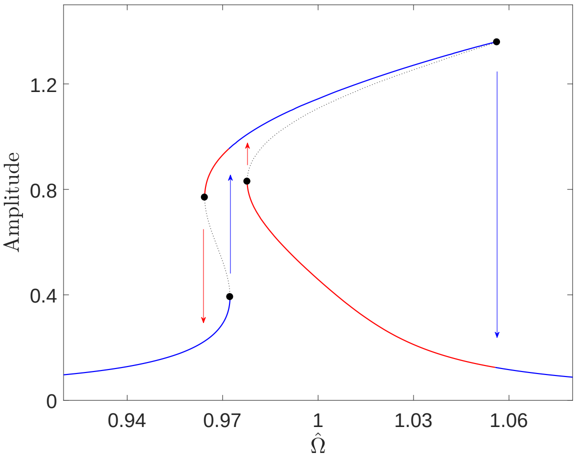

Figure 4.6: Simulated frequency response curve of a SDOF harmonic oscillator, turning from softening into hardening. The experimental forward sweep gives as a solution the blue lines. The remaining parts of the stable solutions, coloured red, can be obtained by performing a backward sweep. The unstable solutions cannot be found experimentally.

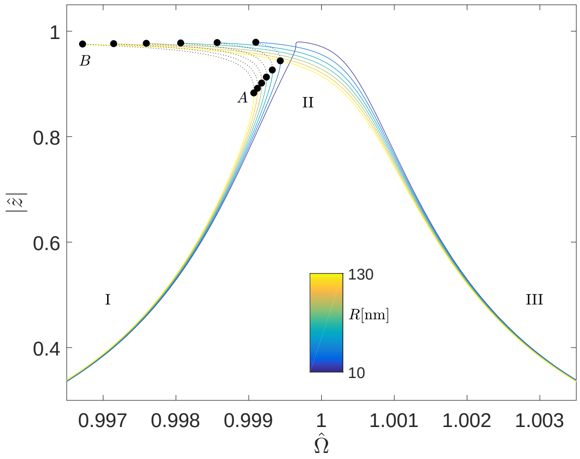

Figure 4.7: Frequency response for different values of the tip radius R (from blue to yellow $R = \{10, 130\}\,\mathrm{nm}$). For the numerical simulation, $z_\mathrm{c} = 20\,\mathrm{nm}$ and a Hamaker constant between a Silicon (Si) tip and a Highly Oriented Pyrolytic Graphite (HOPG) sample $H_{\mathrm{Si-HOPG}} = 2.9656 \times 10^{-19}\,\mathrm{J}$ was considered. This figure is adopted from a publication in Applied Physics Letters, for which I have performed the numerical simulations [1].

The goal is to perform frequency sweeps in the attractive regime, maximizing the influence of the tip radius. Recalling Eq. (3.2), the dimensionless equation of motion of the cantilever under sole influence of van der Waals forces is

$$\frac{\partial^2 \hat{z}}{\partial \tau^2} + \hat{c}\frac{\partial \hat{z}}{\partial \tau} + \hat{z} = \lambda \cos(\hat{\Omega}\tau) - \beta \frac{1}{(1+\hat{z})^2}. \tag{4.2}$$

The term $\frac{1}{(1+\hat{z})^2}$ characterizes a softening nonlinearity, whose magnitude is governed by $\beta = \frac{HR}{6z_\mathrm{c}^3 k_\mathrm{c}}$. It is important to analyze the effect of the tip radius on the frequency response of the cantilever. Assuming R as a sole varying parameter in Eq. (4.2), the frequency response as a function of the tip radius is reported in Fig. 4.7. The frequency response in the attractive regime shows a softening behaviour, with a saturation towards $|\hat{z}| = 1$, which indicates the position of the sample surface. The large values of the tip radius affect the position of the saddle-node points (points A and B, respectively), bending the peak of the response towards lower frequencies. In point B the biggest alterations are observed. Interestingly, it seems that for linear step variations of the tip radius, the value of the resonance peak changes linearly as well.

In order to construct a frequency sweep that can be compared to numerical simulations, a lot of experimental factors need to be considered. Inspection of Eq. (4.2) gives an insight that besides R, other parameters contribute to the nonlinear response. Proper identification of the attractive regime is and added challenge and depends on many aspects as well. It is necessary that an experimental operating region is found where the softening in the frequency response is as high as possible. This region can be found by constructing an experimental backbone curve.

4.3. Experimental Procedure

Each time a quantitative experiment is performed, the stiffness k_c, the first resonance frequency ω_n and the quality factor Q for the free vibrating cantilever are calibrated based on its Brownian motion. The Hamaker constant defines the van der Waals body-body interaction between tip and sample, which can be derived from the values of $H_{\text{air-tip}}$ and $H_{\text{air-sample}}$. Let's define H_{132} as the Hamaker constant for media 1 and 2 interacting across medium 3. H_{132} can be approximated by

$$H_{132} = (\sqrt{H_{11}} - \sqrt{H_{33}})(\sqrt{H_{22}} - \sqrt{H_{33}}), \tag{4.3}$$

where H_{11}, H_{22} and H_{33} are the Hamaker constant of medium 1,2 and 3, respectively, whose values can be found in the literature [55, 86].

Furthermore, the distance between the probe rest position and the sample z_c is an important parameter, due to the fact that magnitude of the softening nonlinearity β has a dependency on z_c^{-3}. For this reason, experimentally it is necessary to maintain a known constant z_c or know it's value at every measurement point. Control of z_c in theory might seem an elementary task, but turns out to be very hard in practice. A simple option to maintain a constant rest position from the sample is not available in the FLEX AFM system. In order to obtain the frequency response curves accurately and in a repeatable manner, a systematic method needs to be defined.

4.3.1. Procedure 1: 'Tip Lift'

The first method that was developed is based on a novel feature available in the FLEX AFM. There are a number of imaging modes available in the AFM, shown in Fig. 4.8. A topographic image is obtained by means of raster scanning the sample. The operating modes consist of a forward and a backward scan. In the standard mode, the Z-controller is enabled during both forward and backward scan. With the dual scan mode, the first forward and backward scan is made in the standard setting, but then a second scan is made with the Z-controller disabled. In the interlaced mode the Z-controller is enabled in the forward scan and disabled in the backward scan. In the second scan only mode, the Z-controller is only enabled before the start of each scan. The C3000 controller of the FLEX AFM contains an option called 'second scan tip lift', making it possible to move the cantilever base upwards after the first scan with a specified distance. In the first scan, the sample finds a certain set-point and during the second scan, the tip moves to a specified distance above the sample and a scan is performed.

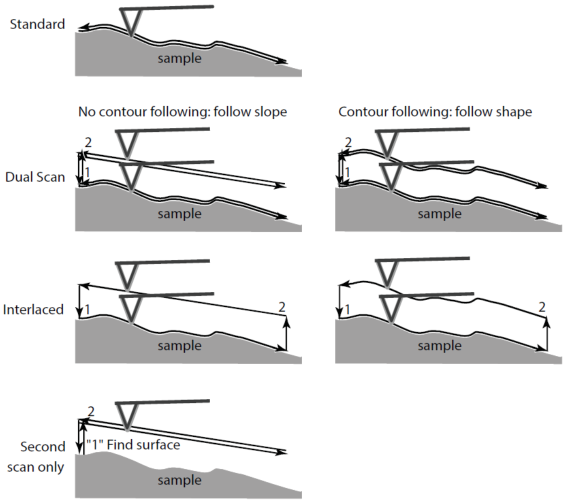

Figure 4.8: The available imaging modes in the AFM. The operating modes consist of a forward (1) and a backward (2) scan. The standard mode follows the sample in both the first and second scan. The dual scan mode allows the user to follow a slope or the sample contour during the second scan. With the interlaced mode the forward and backward scan can be decoupled. In the second scan only, the surface is found with the first scan, and the second scan is carried out following a slope.

Using the second scan tip lift, a systematic method was developed to perform frequency sweeps at a specified distance above the sample. The image scan size was set to 0 × 0 nm, with the purpose to maintain a constant position in the X-Y plane and to perform repetitive scans at a single point on the sample. The scans are carried out in the static mode and a deflection set-point is found during the first scan. The amount of time it takes to complete a point measurement was adjusted to be slightly longer than time it takes to perform a single sweep. A frequency response measurement with the ’tip lift’ is executed as follows:

1. An imaging measurement in the static mode was started;
2. After the Z-controller has found the set-point in the first scan, the cantilever was moved upwards and the second scan started;
3. As soon as the second scan was started, the forward frequency sweep was performed;
4. After the frequency sweep had finished, step 3 was repeated and the backward sweep was carried out;
5. The imaging measurement was stopped.

The way to validate the procedure is to check its repeatability and accuracy. Accuracy is analyzed by constructing an experimental backbone curve, created by performing multiple frequency sweeps for increasing values of the excitation amplitude. The repeatability was investigated by carrying out multiple frequency sweeps while keeping all parameters constant.

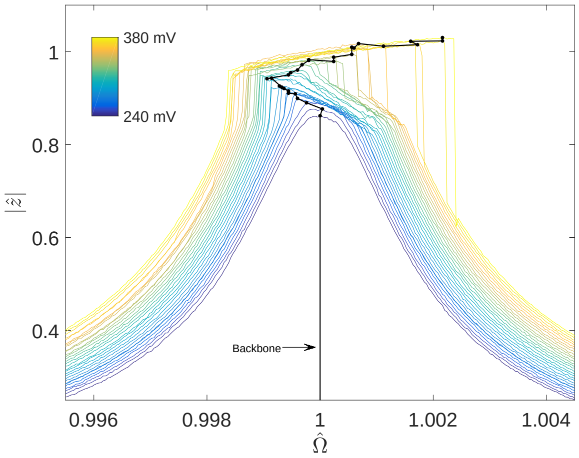

Figure 4.9: Experimental backbone curve obtained with the ’tip lift’ procedure, performed on a mica sample, $z_c \approx 30\,\text{nm}$. The color code indicates an increase in excitation.

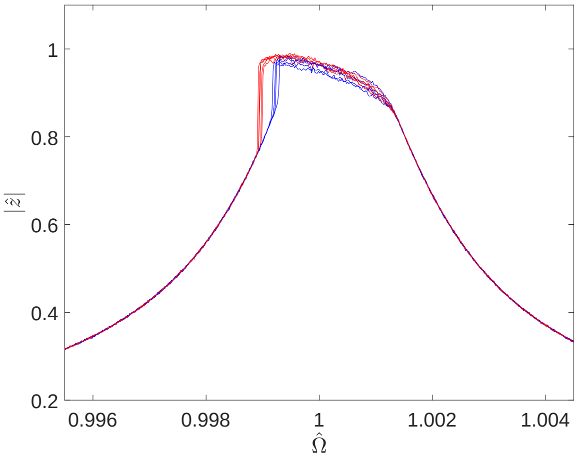

Figure 4.10: Multiple forward (blue) and backward (red) sweeps performed with the ’tip lift’ procedure and a constant driving force.

The backbone curve in Fig. 4.9 constructed from the sequential frequency sweeps shows a clear softening turning into hardening. The force steps can be controlled very accurately, as can be in observed in the plot. One can notice that when there is nonlinear interaction between tip and sample, the instability increases. There even is overlap between certain curves in these regions, which does not cohere with theory. Due to the fact that the Z-controller is switched off during the second scan the cantilever base is free to be influenced by external effects, causing drift in the Z-direction. Especially when the scan time is increased, the drift increases. It was also observed in other experiments that, probably due to the interaction forces, the drift shows a clear direction. More examples of the drift in the sequential frequency response curves are available in Appendix B.6.

The repeatability of the method, at least for short scan times, is fairly acceptable. In Fig. 4.10, multiple forward and backward sweeps with constant excitation in a single session are plotted. The large jumps are associated with the backward sweep and the smaller jumps with the forward sweep. There are many possible causes for the small variation in the location of the saddle node points between the different sweeps, the most likely being the alterations in z_c, due to the absence of control in the Z-direction. Once again, it is clear that in the nonlinear region of Fig. 4.9, where the resonance curve flattens, there is a lot variation between the curves. It is speculated that the deviations are a result of the attractive forces affecting z_c. For these reasons this method is incapable of maintaining a consistent defined distance from the sample and is discarded. However, the method could be useful in further research, as new developments and upgrades from the AFM manufacturer’s side can provide more advanced and different techniques to aid the ’tip lift’ technique. Better control on the Z-axis could contribute to a successful experimental methodology. A previous study successfully implemented a similar procedure to achieve noncontact operation and performed a parametric study [52].

4.3.2. Procedure 2: 'Z-Axis Closed-Loop-Control'

The results from the 'tip lift' method pointed out that control over z_c during the frequency sweep is required. In the AFM software, the static force-spectroscopy allows for specification of the approach and retract distance from the sample. Static force-spectroscopy can serve as a tool to find the 'zero' value, i.e. the sample, and can also be used to retract with a certain distance. An added advantage of using force-spectroscopy is that the amount of force with which the tip indents the sample can be specified, and thus be set very low, limiting the amount of damage that is done to the tip. The retract distance can be maintained by using a feature of the AFM system, called the 'Z-closed-loop', which can keep a steady position if the AFM is not scanning or moving in the Z-direction during spectroscopy. In other words the last value of the Z-position of a spectroscopy can be maintained with this feature. After the cantilever base has retracted the specified distance from the set-point, the closed loop can be activated instantly and the current Z-position will act as the reference value. When the closed loop is activated, the AFM is operating in an idle mode, where the AFM scanner can't perform scanning or spectroscopy. With the external drive however, frequency sweeps can still be performed. With addition of the closed loop control on the Z-axis a new systematic procedure is defined:

1. In the static mode, the cantilever was approached (approach phase);
2. a force-distance curve was acquired recording the effective deflection of the cantilever. The forward motion was stopped at a small cantilever deflection set-point;
3. The cantilever was pulled back from the sample with a fixed backward length (retract phase);
4. The closed-loop controller on the Z-axis motion was activated to avoid drifting away from the specified position;
5. The frequency was swept forward and backward in the specified neighbourhood of the estimated resonance frequency and the vibrational amplitude was measured.

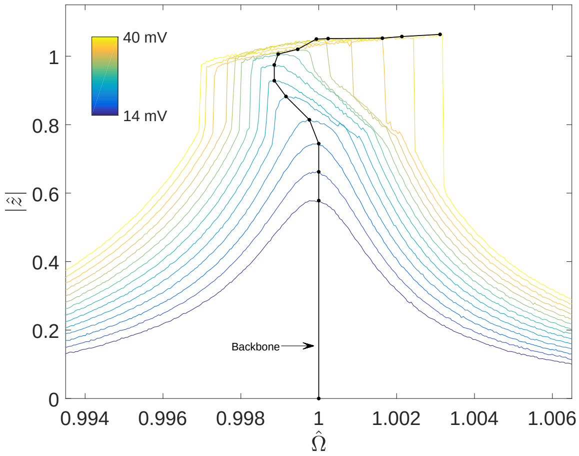

Figure 4.11: Experimental frequency response curve with increasing excitation amplitude. The color code indicates an increase in excitation (2 mV steps were made). The solid line indicates the backbone curve, and the sample is at $z_c = 20$ nm. This figure is adopted from a publication in Applied Physics Letters [1]. The experiments have been performed by E. Rull Trinidad and myself.

This procedure is evaluated with a similar approach as before. The accuracy is checked by constructing the experimental backbone curve. With the new procedure the backbone looks much smoother. There is less instability in the nonlinear regions, and there is a clear gradual transition from softening turning to hardening. Note that this backbone was made at $z_c = 20$ nm in contrast to the backbone in Fig. 4.9, which was made at $z_c = 30$ nm. The transition between softening and hardening compresses for increasing values of z_c, which adds to the difference between the two experiments. The repeatability is comparable to the 'tip lift' method, but especially in the nonlinear regions this procedure provides more stability, as it is repeatedly able to follow the upper part of the resonance curve without any large alterations.

A single force-spectroscopy covers steps 1, 2 and 3 of the procedure. The sample is approached statically until a certain deflection set-point is found. The value of this deflection is chosen by compromise. On one hand it must not be too large, as the risk of initial tip damage is then further increased. On the other hand it may not be too small. The sample needs to be identified, so the set-point must be higher than the deflection caused by the peak attractive force. If this condition is not satisfied, a set-point could be found somewhere above the sample. Also, the deflection must be high enough to be controllable, as too small set-points can cause instability in the control.

4.4. Identification Process

For the identification process, the properties of the cantilever and sample are assumed to be known. Experimentally obtained frequency curves will be compared to simulations, using a nonlinear fitting procedure. The regions I and III in Fig. 4.7 are primarily determined by the excitation force F_0 and region II, the width of the curve, is dominated by the quality factor Q. Next, the positions of the saddle node points connecting the stable and unstable motion were matched considering the tip radius as the sole fit parameter. Due to the softening nature of the frequency response, obtaining the data from the backward sweep was crucial for the fitting. This permits to find the saddle node point B, corresponding to the maximum amplitude. A precise match of saddle node B is prioritized due to the fact that B shows a more significant change for changing values of R than point A. It has to be remarked that the implemented model analyzes the cantilever motion only for attractive interaction ($d > a_0$). The quality factor of a nonlinear fitting would be lower with respect to its calibrated value, this is due to the effect of nonlinear energy dissipation [87]. An estimated uncertainty in z_c of $\pm 1\,\mathrm{nm}$ was taken into account. Additionally a fitting error of around $F_0 \pm 4\,\%$ is considered. An estimation of the tip radius with reasonable accuracy while accounting for these uncertainties and error margins would demonstrate the robustness of the method.

The bifurcation analysis package AUTO is not easily compatible with other programming languages and sequential simulation data cannot be stored efficiently. Consequently, the implementation of an iterative, numerically based and time-efficient fitting procedure is a difficult task. The possibility of implementing an automated identification algorithm based on harmonic balance in MATLAB has been investigated. The theoretical analysis is found in Appendix A.2. For these results a brute force approach has been chosen. The uncertainties for z_c were selected at the boundaries, 5 or 6 values between $F_0 \pm 4\,\%$ are defined and the range of quality factors $Q_1, \ldots Q_n$ are rounded to integer values with the purpose to decrease the computational time by maintaining an acceptable accuracy.

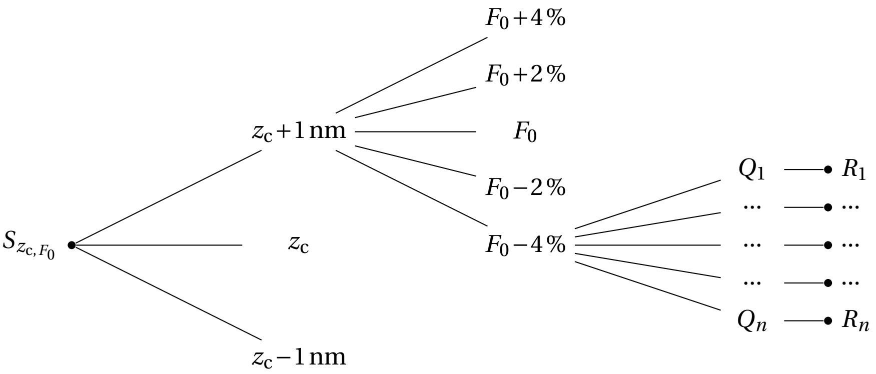

Figure 4.12: Branch diagram, visualising the brute force fitting procedure, starting from the optimal fit S_{z_c,F_0}. In a typical fitting procedure 4 values for Q are found where the saddle node points can be matched properly. Often, more than 60 simulation iterations are performed before a single fitting procedure is completed.

4.5. Validation with SEM

The proposed method is verified by comparing the results to SEM. A limitation of the SEM is that only semi-quantitative information of the tip shape can be collected. By reviewing research on tip wear characteristics, it is found that it is customary to obtain a value for the tip radius in SEM by means of fitting a circular shape to the tip apex. However, values for tip radii extracted from SEM images have been reported without further clarification on how these are retrieved [45]. Because the circles are drawn by naked eye, fits with different radii can be made. The range of R with which these circles are composed will be used as a comparison to the fitting procedure. Note that the circular fits are not obtained by constructing a circle inside the tip apex but rather by following the outer contour of tip that interacts with the sample, as demonstrated in Fig. 4.13.

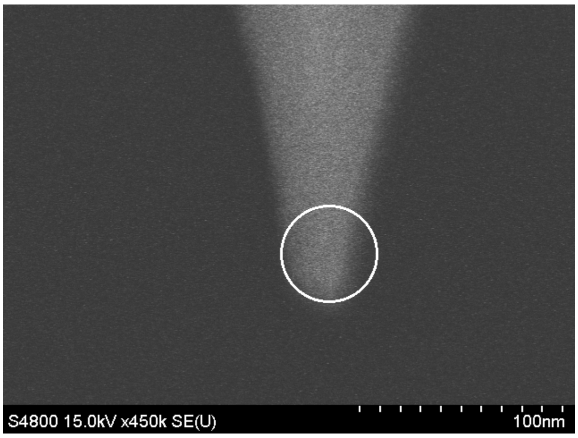

Figure 4.13: SEM image of the cantilever tip. The proposed circular fit follows the part the tip that interacts with the sample.

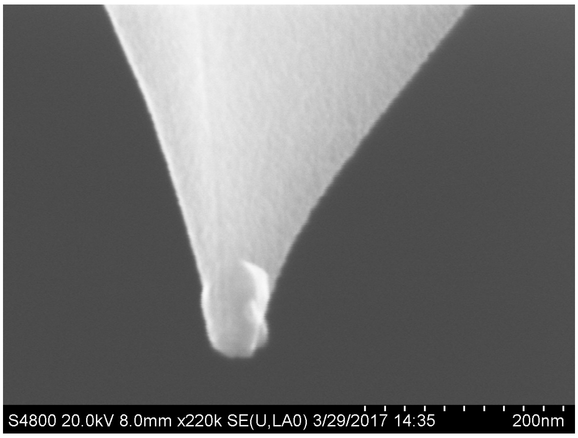

Figure 4.14: SEM image of an AFM tip with contamination at its sharp end.

The SEM can give an indication of the tip apex shape, if it is indeed (hemi-)spherical or not. More importantly one can observe if there are any signs of breakage or contamination on the tip, as shown in Fig. 4.14. The latter is especially relevant, as with non-optical procedures it's complicated to predict if the tip is contaminated. More information about experiments with contaminated tips can be found in Appendix B.1. When fragments of the sample remain on the tip apex, the Hamaker constant between the two bodies will change, modifying the van der Waals interaction.

5

Results

The experiments used for the fitting procedure were performed with new cantilevers and thus 'fresh' tips. It has to be stated that initial measurements and calibrations which require contact between tip and sample cannot be avoided. To minimize further dangerous tip damage and to maximize the influence of the tip radius it is important to identify the noncontact, or attractive regime. This is done by sweeping the excitation frequency at constant z_c from below to above resonance for increasing values of the excitation force F_0, until right before the point where repulsive forces influence the response, herewith maximizing the softening nonlinearity. After the decisive experiments have been performed, the cantilever was removed from the AFM scan-head. It was made sure that additional contact with the sample or any other surface was avoided. For the definitive experiments, the NCLR type cantilever and a Highly Oriented Pyrolytic Graphite (HOPG) sample was used. The main motivation for picking this sample is that compared to other samples, the combined Hamaker constant of $H_{\mathrm{Si-HOPG}} = 2.9656 \times 10^{-19}$J is relatively high, which as a result maximizes the nonlinear interaction β. (The results presented in this section led to a publication in Applied Physics Letters, for which I have performed the numerical simulations [1]. The authors jointly used them to interpret the experimental data measured by E. Rull Trinidad. The SEM images shown in this section are acquired by E. Rull Trinidad. Complete tables of the fitting results can be found in Appendix B.4.)

5.1. Experiment 1

The first experiment was performed at $z_c = 20\,\mathrm{nm}$. The experimental curves in Fig. 5.1 could be fitted with a (hemi-)spherical tip radius of $R = 19 \pm 6\,\mathrm{nm}$. The value found in the fitting is in good agreement with the obtained value from the SEM image, which gives $R = 18 \pm 2.7\,\mathrm{nm}$.

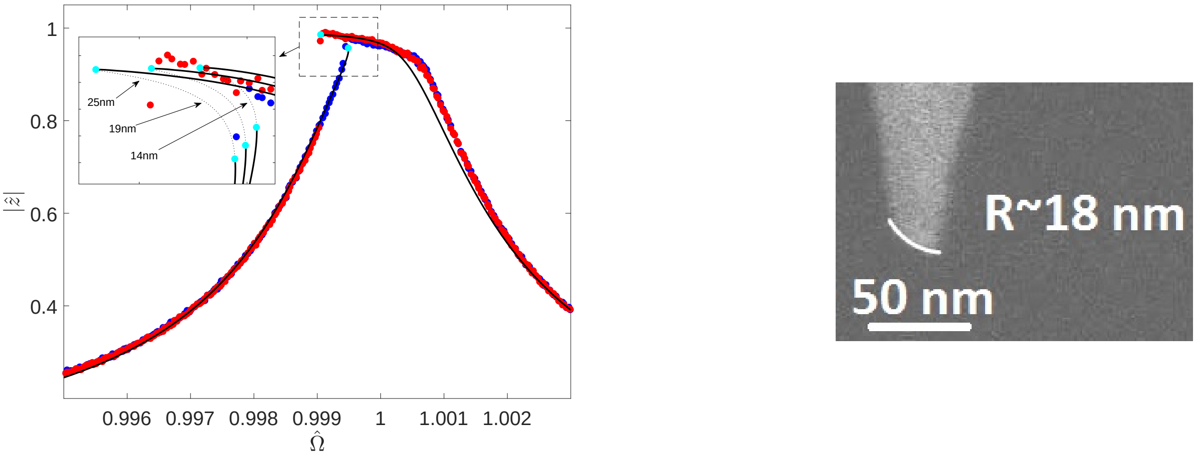

Figure 5.1: LEFT: Forward (blue dots) and backward (red dots) experimental frequency response curves with a proposed numerical fitting (black line) of $R = 19\,\mathrm{nm}$. The small inset graph targets the saddle node points (light blue dots) and contains simulated curves of the upper and lower bound retrieved from the fitting. RIGHT: SEM image of the corresponding AFM tip. The numerical simulation for $R = 19\,\mathrm{nm}$ was performed with $Q = 387$, $F_0 = 1.325\,\mathrm{nN}$, $z_c = 20\,\mathrm{nm}$, $\omega_n = 166878\,\mathrm{Hz}$ and $k_c = 26\,\mathrm{N\,m^{-1}}$.

5.2. Experiment 2

The second experiment was performed at $z_\mathrm{c} = 25\,\mathrm{nm}$. The SEM image in Fig. 5.2 reveals that the tip apex is blunted. For this case a flat-circular tip model would provide a better approximation of the tip-sample geometry. Recalling from Table 2.1, the van der Waals forces for a flat-circular tip with radius r and a flat sample surface is equal to

$$F_\mathrm{vdW}(z, z_\mathrm{c}) = -\frac{Hr^2}{6(z_\mathrm{c}+z)^3}. \tag{5.1}$$

The dimensionless equation of motion for this tip-sample geometry is

$$\frac{\partial^2 \hat{z}}{\partial \tau^2} + \hat{c}\frac{\partial \hat{z}}{\partial \tau} + \hat{z} = \lambda \cos(\hat{\Omega}\tau) - \beta \frac{1}{(1+\hat{z})^3}, \tag{5.2}$$

where the magnitude of the nonlinear interaction is governed by $\beta = \dfrac{Hr^2}{6z_\mathrm{c}^4 k_\mathrm{c}}$. The tip radius estimation of $r = 12 \pm 1.5\,\mathrm{nm}$ in Fig. 5.2 was obtained accounting for the flat-circular (blunted) tip interaction, which is good agreement with the SEM image, where a flat-circular tip with $r = 10 \pm 2\,\mathrm{nm}$ could be found. Note that, by applying the (hemi-)spherical model to this set of experiments, a radius of $R = 60 \pm 18\,\mathrm{nm}$ was obtained.

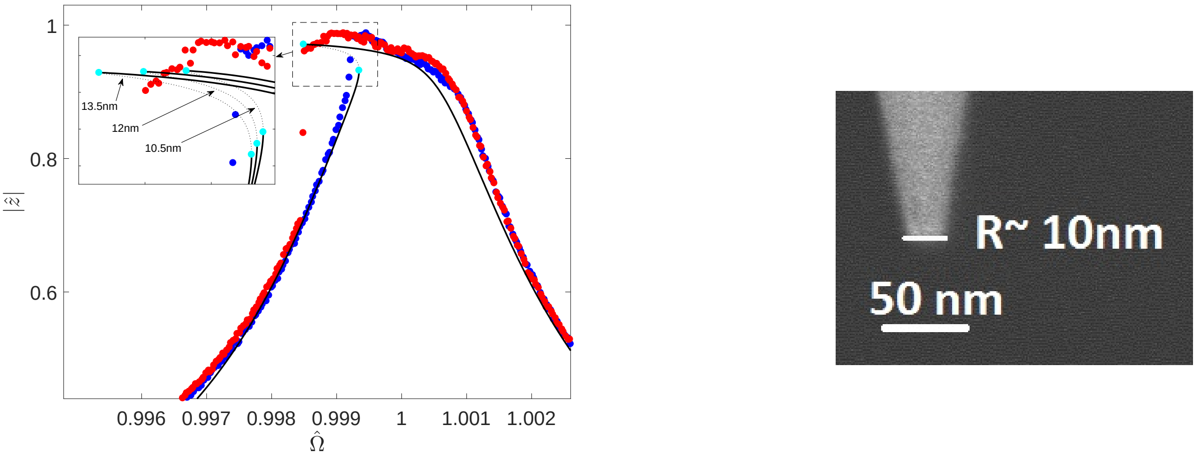

Figure 5.2: LEFT: Forward (blue dots) and backward (red dots) experimental frequency response curves with a proposed numerical fitting (black line) of $r = 12\,\mathrm{nm}$. The small inset graph targets the saddle node points (light blue dots) and contains simulated curves of the upper and lower bound retrieved from the fitting. RIGHT: SEM image of the corresponding AFM tip. The numerical simulation for $r = 12\,\mathrm{nm}$ was performed with $Q = 312$, $F_0 = 1.95\,\mathrm{nN}$, $z_\mathrm{c} = 25\,\mathrm{nm}$, $\omega_\mathrm{n} = 164973\,\mathrm{Hz}$ and $k_\mathrm{c} = 25.3\,\mathrm{N\,m^{-1}}$.

6

Discussion

6.1. Evaluation of the Results

Both results show good agreement with their corresponding SEM image. The first experimental curves could be fitted with the (hemi-)spherical tip model, and the other tip estimation could be obtained accounting for a blunted tip (flat-circular) interaction. By applying the (hemi-)spherical model to the last set of experiments, a discrepancy between the SEM image and the identified tip radius is observed. However, the order of magnitude remains preserved ($R \approx 60\,\mathrm{nm}$). This emphasizes that the (hemi-)spherical model could serve as a precautionary model if an *in-situ* estimation of the tip is to be performed, it provides a more secure limit for avoiding excessive tip deterioration.

6.2. Validation of the Method

The amount of experimental data acquired is not sufficient to properly analyze the accuracy and repeatability of the proposed methodology. The lack of result is related to experimental conditions and the extreme sensitivity of AFM tips. It is very difficult to determine the specific experimental environment where the AFM tip remains intact. It is found that even a slightly too deep indentation into the sample can cause excessive deterioration, contamination or even breakage of the tip. Some of the current methods for tip characterization which demand further tip-sample contact after definitive measurement do not take these potential consequences into account.

Throughout the course of the experiments, it was observed that the response of some cantilevers was somewhat irregular, even linear frequency response curves without softening or hardening were difficult to match with numerical simulations, for examples see Appendix B.5. The asymmetry in the curves could be related to improper positioning of the laser, imperfect mounting of the cantilever on the scan head or irregularities in its geometry. The fitting procedure is difficult to apply when the cantilever response is noticeably affected, as the model assumes symmetry in the shape, and it does not yet incorporate the physical effects of laser positioning and cantilever mounting on the cantilever response.

The proposed method is verified by comparing the results to SEM, where information of the tip shape is only semi-quantitative. In one of the experiments the static force-spectroscopy measurement was also obtained and a fit could be achieved that was within the tolerances of the dynamic method [1]. It would be desired to determine the size of a single tip with multiple characterization methods and compare the outcome. However, most of these require additional dangerous tip-sample contact, hence their results will be incomparable.

7

Recommendations & Conclusion

7.1. Recommendations

7.1.1. Implementation of a Nonlinear System Identification Algorithm

A brute force fitting approach was followed instead of a nonlinear system identification method such as harmonic balance, which is at the expense of accuracy. A proper numerical algorithm with a defined error function could provide a more precise and robust estimation. The lock-in amplifier is not yet capable of obtaining the frequency response for multiple modes simultaneously, thus for numerical identification methods, only frequency-amplitude data near the first mode or driving frequency would be available. Realisation of an sophisticated system identification algorithm will provide the next step towards true *in-situ* tip estimation.

7.1.2. Exploiting Higher Harmonics & Intermodulation Products

The implemented experimental procedure could also be applied for the extraction of higher harmonics. The harmonic signals could also be amplified by using a more compliant type of cantilever. In order to find a more universal approach, this option was not explored in this work.

Deliberate excitation of multiple frequencies at once might also lead to new insights about the tip-sample interaction. It has been shown that other frequencies, known as intermodulation products, are generated when the cantilever is perturbed by the nonlinear tip-sample interaction. The multi-frequency lock-in amplifier is especially suited for the acquisition of these intermodulation signals, which is why it could be an interesting direction for further research.

7.1.3. True Tip Shape Determination

It is fairly accepted in the AFM field that the tip geometry is approximated as a continuum body. This assumption allows one to describe the interaction forces with relative ease by using continuum mechanics models. For most applications in AFM a more rigorous determination of the tip shape is no necessity, as long as the tip is sharp enough. But as future research will advance to even smaller scale, precise characterization of the tip apex will be required. In the proposed method a certain tip geometry is assumed and the optimal characteristic value for that shape is found. But the tip shape itself could also serve as a source of optimization. The Blind Tip Reconstruction is roughly based on this principle and could be a source of inspiration to further research. Instead of assuming a predefined tip geometry in the model, the tip shape could be determined with topology optimization. Besides continuum mechanics, a model based on molecular dynamics could be implemented to describe the tip-sample interaction on a true atomic level.

7.1.4. Future Research and Outlook

It is known that the repulsive forces in AFM are generally stronger than the attractive forces. For this reason it is realistic that parameter estimation in the repulsive regime is feasible. This would require the inclusion of contact forces in the theoretical model. In order to reach true noncontact *in-situ* tip identification, additional tip-sample contact needs to be avoided.

Using higher harmonics as a source of the nonlinearity is still a promising solution, as they could be extracted whilst performing other measurements, and could be a focus point for further research. A novel approach that could be explored is to assemble a tip with a known geometry on the AFM cantilever. This takes away uncertainty about the tip shape. Furthermore, the future of AFM is tending towards the development of AFM probes capable of true 3D measurement, where instead of a cantilever a membrane is used. Because tips need to be fabricated on these membranes, preliminary research on conventional AFM cantilevers can contribute to new insights.

7.2. Conclusion

To conclude, nonlinear dynamics can certainly be used to estimate the tip condition in AFM. Analysis of the tip-sample mechanics and nonlinear dynamics pointed out that the influence of the tip radius is predominant in the attractive regime. A methodology to determine the tip radius in AFM has been presented and consists of the acquisition of frequency response curves in this attractive regime and a nonlinear fitting procedure is used to match the experimental curves in order to estimate the tip radius. There are still enough areas that require improvement. Experimental uncertainties need to be minimized or either considered in the model and a deterministic fitting procedure has to be implemented, which would make the method more accurate and robust. Moreover, approximation of the tip geometry in the theoretical model is a limitation for true tip shape determination. The presented methodology is a first step towards automated *in-situ* tip identification, estimation of material properties and could serve as an inspiration for novel techniques in future AFM systems.

A

Analytical Descriptions

A.1. Dimensionless Equation of Motion

In this section the dimensionless equation of motion for an AFM cantilever subjected to tip-sample interaction forces is derived. The following assumptions are made:

- The cantilever-tip ensemble is modelled as point-mass spring system;
- The quality factor is independent from tip-sample separation;
- The tip-sample geometry is approximated with a (hemi-)sphere and a flat surface;
- The cantilever is excited by means of a singular periodic excitation;
- The cantilever base is stationary with a distance z_c separated from the sample.

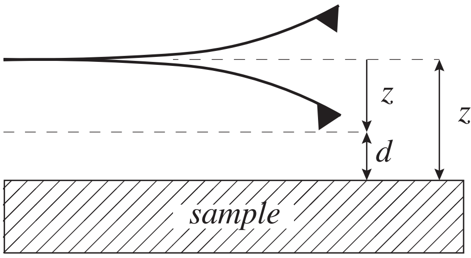

Figure A.1: Free body diagram of the AFM cantilever and the sample. The rest position of the cantilever acts as a reference for the deflection z.

The general equation of motion for the one-dimensional system is:

$$m\frac{\partial^2 z}{\partial t^2} + c\frac{\partial z}{\partial t} + k_\mathrm{c} z = F_0 \cos(\Omega t) + F_\mathrm{ts}. \tag{A.1}$$

Here m, k_c, F_0 and F_ts are the tip mass, cantilever stiffness, excitation force and the net tip-sample interaction force, respectfully. The damping c is equal to

$$c = \frac{m\omega_\mathrm{n}}{Q}, \tag{A.2}$$

where ω_n is the cantilever's first resonance frequency and Q it's quality factor. Assuming the DMT model, the tip sample forces can be described by

$$F_\mathrm{ts}(d) = \begin{cases} -\dfrac{HR}{6d^2}, & d > a_0 \\ -\dfrac{HR}{6a_0^2} + \dfrac{4}{3}E^*\sqrt{R}(a_0 - d)^{\frac{3}{2}}, & d \le a_0. \end{cases} \tag{A.3}$$

Here H, R, d, E^* and a_0 are Hamaker constant, the tip radius, the instantaneous tip-sample separation, the effective Young's modulus and the intermolecular distance, respectfully.

The above equation can be made dimensionless. The characteristic length is $\hat{z} = \frac{z}{z_\text{c}}$ and the characteristic time is $\tau = \omega_\text{n} t$. The equation can then be made dimensionless as

$$m\omega_\text{n}^2 z_\text{c} \frac{\partial^2 \hat{z}}{\partial \tau^2} + \frac{m\omega_\text{n}^2 z_\text{c}}{Q}\frac{\partial \hat{z}}{\partial \tau} + k_\text{c} z_\text{c} \hat{z} = F_0 \cos(\hat{\Omega} t) + F_\text{ts}, \tag{A.4}$$

where λ is the dimensionless excitation force. Recall that for a linear mass spring system $\omega_\text{n} = \sqrt{\frac{k_\text{c}}{m}}$. Divide by $k_\text{c} z_\text{c}$ and express the spatial parameters in $\hat{z}$ and z_c:

$$\frac{\partial^2 \hat{z}}{\partial \tau^2} + \frac{1}{Q}\frac{\partial \hat{z}}{\partial \tau} + \hat{z} = \frac{F_0}{k_\text{c} z_\text{c}} \cos(\hat{\Omega} t) + \frac{F_\text{ts}}{k_\text{c} z_\text{c}}, \tag{A.5}$$

with

$$F_\text{ts}(\hat{z}, z_\text{c}) = \begin{cases} -\dfrac{HR}{6z_\text{c}^2}\dfrac{1}{(1+\hat{z})^2}, & \hat{z} > \dfrac{a_0}{z_\text{c}} - 1 \\ -\dfrac{HR}{6a_0^2} + \dfrac{4}{3}E^*\sqrt{R}\big(a_0 - z_\text{c}(1+\hat{z})\big)^{\frac{3}{2}}, & \hat{z} \leq \dfrac{a_0}{z_\text{c}} - 1. \end{cases} \tag{A.6}$$

The dimensionless equation of motion can then be written as

$$\frac{\partial^2 \hat{z}}{\partial \tau^2} + \hat{c}\frac{\partial \hat{z}}{\partial \tau} + \hat{z} = \lambda \cos(\hat{\Omega} \tau) + \hat{F}_\text{ts}. \tag{A.7}$$

The non-dimensional dissipation coefficient is governed by $\hat{c} = \frac{1}{Q}$, whereas $\lambda = \frac{F_0}{z_\text{c} k_\text{c}}$ represents the sinusoidal excitation with frequency $\hat{\Omega} = \frac{\Omega}{\omega_\text{n}}$. The tip-sample interaction force is then governed by

$$\hat{F}_\text{ts}(\hat{z}, z_\text{c}) = \begin{cases} -\dfrac{HR}{6z_\text{c}^3 k_\text{c}}\dfrac{1}{(1+\hat{z})^2}, & \hat{z} > \dfrac{a_0}{z_\text{c}} - 1 \\ -\dfrac{HR}{6a_0^2 z_\text{c} k_\text{c}} + \dfrac{4E^*\sqrt{R}}{3z_\text{c} k_\text{c}}\big(a_0 - z_\text{c}(1+\hat{z})\big)^{\frac{3}{2}}, & \hat{z} \leq \dfrac{a_0}{z_\text{c}} - 1. \end{cases} \tag{A.8}$$

A.2. Nonlinear Identification Algorithm

In this section a nonlinear identification algorithm is presented, which is largely based on the work of Amabili et al. [87]. The method comprises of a least-squares technique to reconstruct frequency response curves and identify unknown parameters. In order to obtain the amplitude and frequency of the non-linear system the harmonic balance method is used. An attempt has been made to implement the numerical algorithm in MATLAB. In the next section the algorithm is explained analytically. The use of harmonic balance implies the assumption that:

- The response of the system is periodic;
- The response can be expressed as a series of harmonics.

Harmonic balance approximates the solution of Eq. (3.2) with a truncated Fourier series:

$$\hat{z} \approx \hat{z}_N = z_0 + \sum_{k=1}^{N} a_n \cos kt + b_n \sin kt. \tag{A.9}$$

Here N is the order of truncation and $\hat{z}_N$ is the truncated Fourier series representation of $\hat{z}$.

A.2.1. Approximated Solution Using a Truncated Taylor Series

The dimensionless time is now chosen as $\hat{t} = \Omega t$ and the equation of motion is spatially normalized using $\hat{z} = \dfrac{z}{z_\mathrm{c}}$. Because the nonlinear term does not consist of simple polynomials of the generalized coordinate $\hat{z}$ and trigonometric terms, the equation must be rewritten. If the nonlinear term originating from the attractive forces is approximated using a truncated Taylor Series, the system is simplified:

$$r^2 \ddot{\hat{z}} + r\hat{c}\dot{\hat{z}} + q + \beta(1 - 2\hat{z} + 3\hat{z}^2 - 4\hat{z}^3) = \lambda \cos \hat{t}, \tag{A.10}$$

in which $r = \dfrac{\Omega}{\omega_\mathrm{n}}$. By substituting the truncated Fourier series into this equation and equating the coefficients of each of the harmonics, a system of algebraic equations is obtained which relates the frequency ratio r to the amplitudes $\hat{z}_N$:

$$r^2 D^2 S_z + r\hat{c} D S_z + S_z + \beta(1 - 2S_z + 3P_z - 4Q_z) = S_f, \tag{A.11}$$

where

$$S_z = \begin{Bmatrix} \hat{z}_0 \\ \hat{z}_1 \\ \hat{z}_2 \\ \vdots \\ \hat{z}_N \end{Bmatrix}, \quad P_z = \begin{Bmatrix} p_0 \\ p_1 \\ p_2 \\ \vdots \\ p_N \end{Bmatrix}, \quad Q_z = \begin{Bmatrix} q_0 \\ q_1 \\ q_2 \\ \vdots \\ q_N \end{Bmatrix}, \quad S_f = \begin{Bmatrix} 0 \\ 0 \\ \lambda \\ \vdots \\ 0 \end{Bmatrix}, \tag{A.12}$$

with

$$p_0 = \frac{1}{2\pi}\int_0^{2\pi} (\hat{z}_N)^2 \mathrm{d}t, \quad p_{2k-1} = \frac{1}{\pi}\int_0^{2\pi} (\hat{z}_N)^2 \sin(kt)\mathrm{d}t, \quad p_{2k} = \frac{1}{\pi}\int_0^{2\pi} (\hat{z}_N)^2 \cos(kt)\mathrm{d}t, \tag{A.13a}$$

$$q_0 = \frac{1}{2\pi}\int_0^{2\pi} (\hat{z}_N)^3 \mathrm{d}t, \quad q_{2k-1} = \frac{1}{\pi}\int_0^{2\pi} (\hat{z}_N)^3 \sin(kt)\mathrm{d}t, \quad q_{2k} = \frac{1}{\pi}\int_0^{2\pi} (\hat{z}_N)^3 \cos(kt)\mathrm{d}t. \tag{A.13b}$$

Substituting for $\hat{z}_N^2$ and $\hat{z}_N^3$:

$$\hat{z}_N^2 = p_0 + \sum_{k=1}^{N} p_{2k-1} \sin kt + p_{2k} \cos kt, \tag{A.14a}$$

$$\hat{z}_N^3 = q_0 + \sum_{k=1}^{N} q_{2k-1} \sin kt + q_{2k} \cos kt, \tag{A.14b}$$

with

$$D = \begin{bmatrix} 0 & 0 & \cdots & 0 \\ 0 & D_1 & \cdots & 0 \\ \vdots & \vdots & \ddots & \vdots \\ 0 & 0 & \cdots & D_N \end{bmatrix}, \quad D_N = \begin{bmatrix} 0 & -k \\ k & 0 \end{bmatrix}. \tag{A.15}$$

We assume that the amplitude $\hat{z}_N$, the frequency ratio r and the harmonic excitation force λ are already known for every frequency step. Now the following system can be solved for every j-th frequency step $r^{(j)}$:

$$\begin{bmatrix} r^{(j)} D S_{z^{(j)}} & 1 - 2S_{z^{(j)}} + 3P_{z^{(j)}} - 4Q_{z^{(j)}} \end{bmatrix} \cdot \begin{bmatrix} \hat{c} \\ \beta \end{bmatrix} = \begin{bmatrix} -r^{2(j)} D^2 S_{z^{(j)}} - S_{z^{(j)}} + S_{f^{(j)}} \end{bmatrix}. \tag{A.16}$$

The system of Eq. (A.16) is essentially in the form of $A_i x = B_i$. The system is over-constraint since we have $(2N+1) \times j$ equations, where N is the order of truncation and j the number of frequency steps. In order to solve this, the linear squares technique can be used, but both the amplitudes and the parameters need to be optimized. This can be done by calculating the pseudo inverse of matrix A_i as follows

$$X = (A_i^T A_i)^{-1} A_i^T \cdot B_i, \tag{A.17}$$

and minimizing the norm of the error

$$E = (A_i \cdot X - B_i) \cdot (A_i \cdot X - B_i)^T. \tag{A.18}$$

A.2.2. Analytical Solution

If the nonlinear term originating from the attractive forces is approximated using a truncated Taylor Series, the system is simplified, but another solution is to multiply the whole equation with the nonlinear term $(1+\hat{z})^2$ instead. This leaves:

$$r^2 \ddot{\hat{z}}(1+\hat{z})^2 + r\hat{c}\dot{\hat{z}}(1+\hat{z})^2 + \hat{z} + 2\hat{z}^2 + \hat{z}^3 + \beta = \lambda \cos(\hat{t})(1+\hat{z})^2. \tag{A.19}$$

To be continued...

B

Additional Results

B.1. Contamination of AFM Tips

B.1.1. Experiments on a Mica Sample

In this section, experiments carried out on a mica sample are discussed. The experiments could be fitted with very large (hemi-)spherical tip radius ($R \approx 1100\,\mathrm{nm}$). Close inspection of the cantilever under the SEM provided an explanation on why this result was obtained.

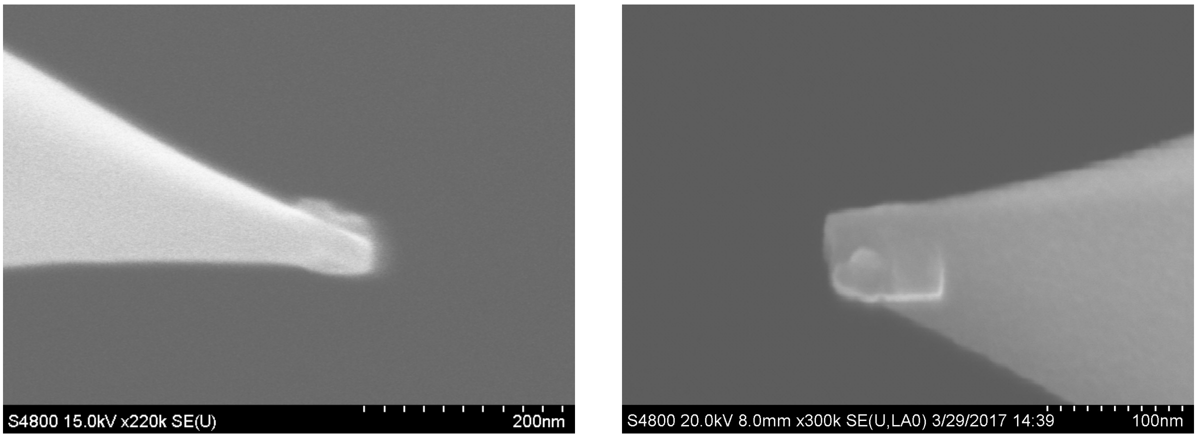

Figure B.1: Two SEM images taken from different sides of the cantilever used in the experiments on the mica sample. The left image shows a clear patch of contamination on the tip. The right image reveals that the tip is blunted.

The SEM images in Fig. B.1 reveal that a patch of contamination has formed on the tip and that the tip apex is far from (hemi-)spherical. In the simulation the tip shape was approximated with a (hemi-)sphere. Similar as the experiment discussed in section 5.2, a flat-circular tip would provide a better approximation for the tip geometry. The proper value for H requires further analysis, because the tip is contaminated with parts of the sample. The tip apex might consist of both mica and Si, further complicating the result and a Hamaker constant of $H_{\mathrm{Si-mica}} = 2.4862 \times 10^{-20}\mathrm{J}$ might be an oversimplified approximation for the van der Waals body-body interaction.

B.1.2. Experiments on a HOPG Sample

Similar problems were observed on the HOPG sample. In one particular experiment, the SEM images were especially intriguing, they are shown in Fig. B.2. Much alike the mica sample, there is a patch of contamination visible on the tip, but also there are flakes of HOPG on its side. This type of contamination could be an outcome of the cleaving procedure of the HOPG sample, which is usually done by sticking a piece of adhesive tape gently to the graphite and then pulling it of again, demonstrated in Fig. B.3. The topmost layer of the sample should then stick to the tape. Large loose flakes can then be removed with tweezers. It is probable that some micro-sized flakes were left on the sample and later picked up by the tip. Due to the many uncertainties this cantilever was considered inapplicable for further analysis.

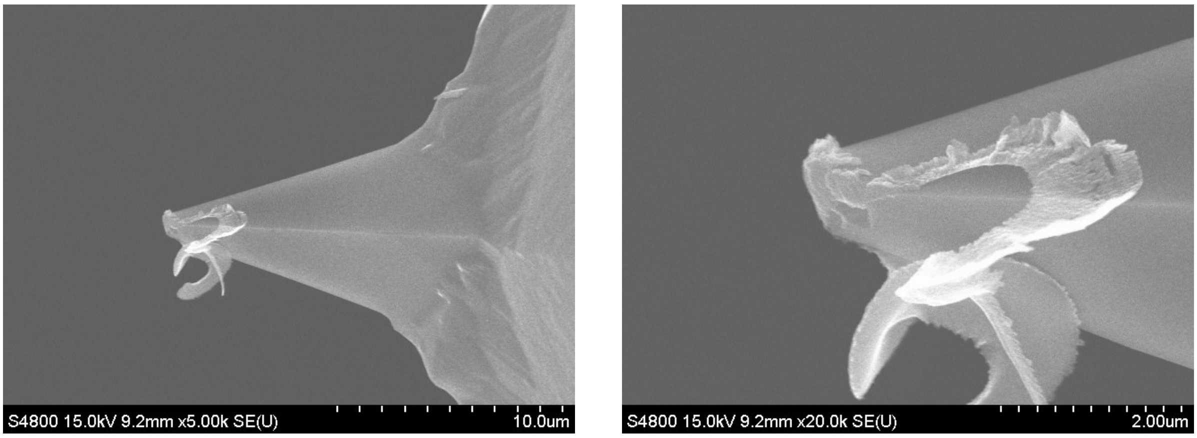

Figure B.2: SEM images of the cantilever contaminated with a patch of contamination and larger flakes of HOPG.

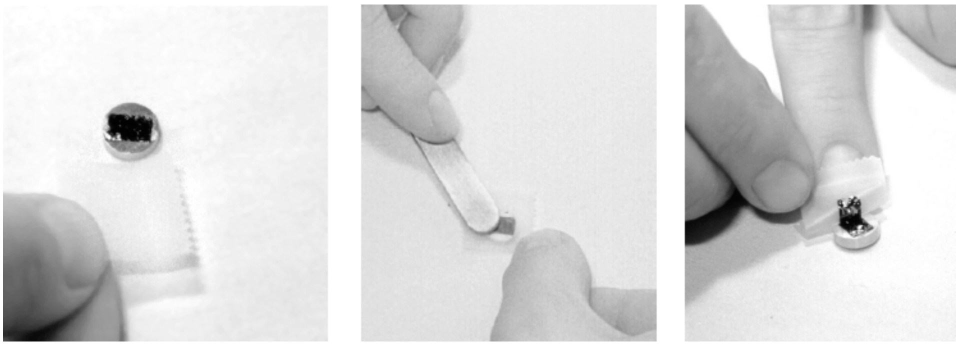

Figure B.3: Cleaving of graphite (source: FLEX AFM operating manual).

These two examples highlight once again that the AFM tips are extremely sensitive. A safe experimental procedure is very hard to find, in some cases the specific cause of contamination or excessive deterioration could not even be traced back.

B.2. Frequency Spectrum of the FMR Cantilever in Different Operating Conditions

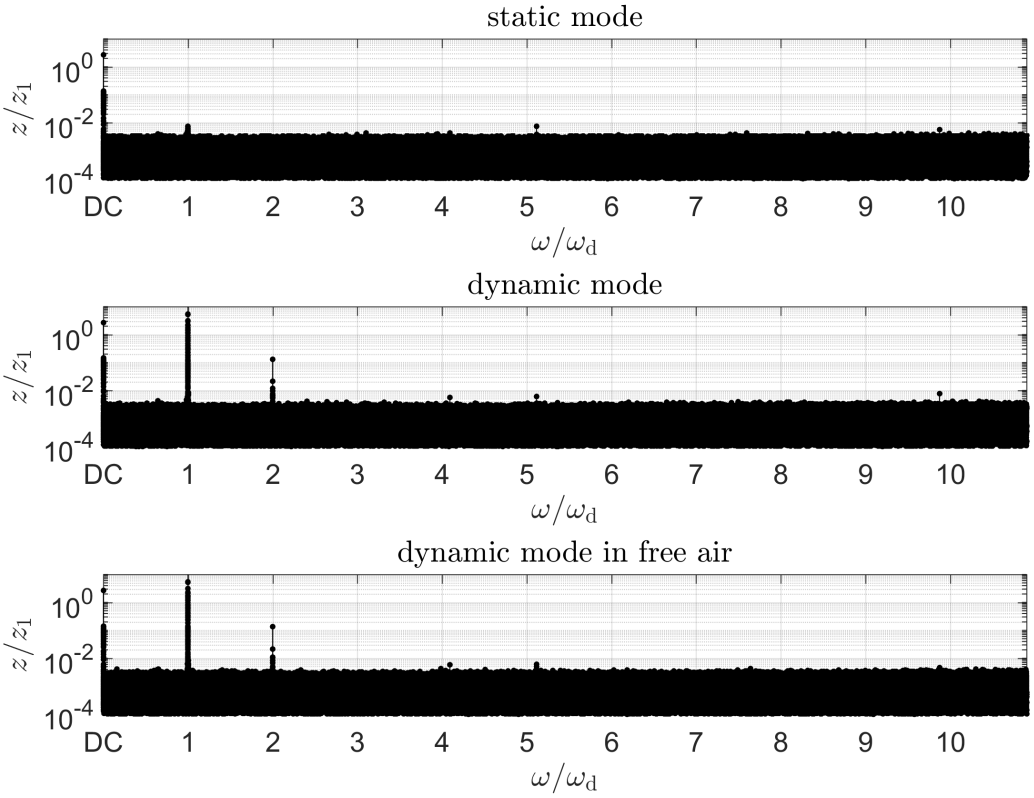

Figure B.4: Experimental frequency spectra of the same FMR cantilever used for the experiment in Fig. 4.4, whilst it scans a sample in the static mode, in the dynamic mode and in free air dynamically.

In Fig. B.4 the frequency spectrum of the FMR cantilever of Fig. 4.4 is plotted whilst scanning the sample in the static mode, in the dynamic mode and whilst scanning in free air in the dynamic mode. In the static mode, no harmonics are being generated, as expected. Interestingly there is little to no difference between the dynamic scanning of the sample and the scanning in free air. The second harmonic is excited for both cases. The conclusion can be drawn that excitation of the second harmonic does not depend on the tip-sample interaction. It has been pointed out in literature that the position of the laser on the back of the cantilever is positioned such that it induces excitation of higher harmonics [41].

B.3. Higher Harmonic Imaging

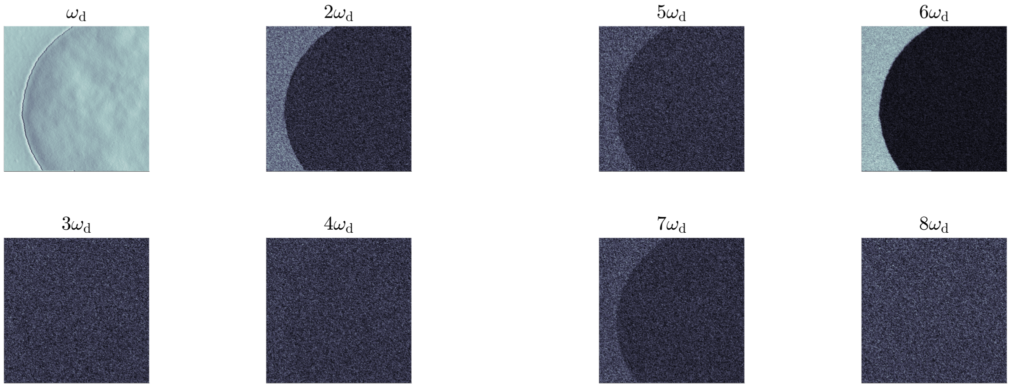

Figure B.5: AM-AFM topography images of PS-LDPE of the driven frequency and several of the higher harmonics. The feedback was performed on the amplitude of ω_d. The higher harmonic images clearly show contrast between the two materials.

The generation of higher harmonics has been investigated in this work in order to find a methodology for tip identification. It was found that the higher harmonic signals were too low and were not suitable for tip estimation, at least for the considered cantilever-sample configurations. However, higher harmonic imaging proves to be useful to monitor the imaging conditions in tapping mode and is often applied to increase the material contrast [83, 84]. Experiments have been performed to demonstrate the working principle of harmonic imaging and are shown in Fig. B.5. The sample used in this experiment consists of two materials, a blend of Polysterene and Polyolefin Elastomer, these materials have a high contrast in elastic modulus (PS-LDPE). The image from the driven frequency ω_d gives a clear indication of the two materials.

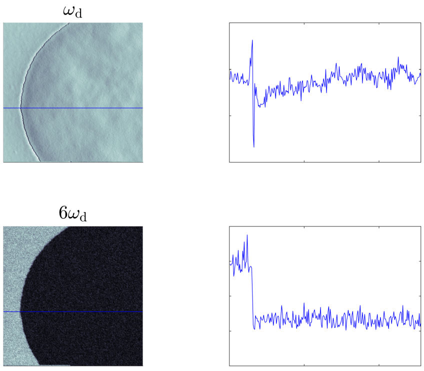

Figure B.6: AM-AFM topography images of PS-LDPE of the driven frequency and its sixth harmonic. One of the scanning lines is highlighted to show the change in the amplitude for both cases. Where the amplitude of ω_d is monitored by the feedback, the amplitude of $6\omega_d$ is free to change.

The feedback is performed on the amplitude of ω_d. In Fig. B.6 it can be observed that the amplitude is more or less constant, except in the part where transition to an other material occurs. No feedback is performed on the higher harmonics thus their amplitude is governed by the tip-sample properties. In the left region the amplitude of $6\omega_d$ is high, but in the right region the amplitude drastically reduces. Te same behaviour is also seen in $2\omega_d$, $5\omega_d$ and $7\omega_d$. This shows that higher harmonics are very useful to increase contrast between different materials in topographic measurements.

B.4. Fitting Results

B.4.1. Experiment 1

Table B.1: Results of the numerical fitting procedure of the first experiment, discussed in section 5.1. LEFT: $z_c - 1 = 19\,\mathrm{nm}$, MIDDLE: $z_c = 20\,\mathrm{nm}$, RIGHT: $z_c + 1 = 21\,\mathrm{nm}$. The tip radii for which a good fit of the saddle node points was obtained are colored green. The tip radii colored red provided a good fit for saddle node B, but saddle node A and the nonlinear part of the curve could not be fitted properly.

$Q[-]$ / F_0 [nN]	1.200	1.225	1.250	1.275	1.300
371					
372					31
373					26
374					21
375					16
376					12
377					8
378					5
379				33	
380				27	
381				22	
382				17	
383				14	
384				9	
385				6	
386			35		
387			29		
388			24		
389			20		
390			16		
391			12		
392			8		
393					
394		35			
395		29			
396		24			
397		20			
398		16			
399		12			
400		8			
401					
402					
403	30				
404	26				
405	21				
406	16				
407	13				
408	10				
409	7				

$Q[-]$ / F_0 [nN]	1.200	1.225	1.250	1.275	1.300
371					31
372					25
373					20
374					15
375					11
376					7
377					
378				31	
379				25	
380				20	
381				15	
382				11	
383				6	
384					
385			32		
386			26		
387			21		
388			16		
389			11		
390			7		
391					
392		34			
393		28			
394		23			
395		18			
396		13			
397		9			
398					
399					
400	32				
401	27				
402	21				
403	17				
404	12				
405	8				
406					
407					
408					
409					

$Q[-]$ / F_0 [nN]	1.275	1.300	1.325	1.350	1.375
371					
372					36
373					30
374					23
375					17
376					12
377					8
378					
379				32	
380				27	
381				21	
382				14	
383				11	
384				6	
385					
386			33		
387			26		
388			20		
389			15		
390			10		
391					
392					
393		33			
394		26			
395		21			
396		16			
397		11			
398		7			
399					
400	35				
401	28				
402	23				
403	17				
404	12				
405	8				
406					
407					
408					
409					

B.4.2. Experiment 2

Table B.2: Results of the numerical fitting procedure of the second experiment, discussed in section 5.2. LEFT: $z_c - 1 = 24\,\mathrm{nm}$, MIDDLE: $z_c = 25\,\mathrm{nm}$, RIGHT: $z_c + 1 = 26\,\mathrm{nm}$. The tip radii for which a good fit of the saddle node points was obtained are colored green. The tip radii colored red provided a good fit for saddle node B, but saddle node A and the nonlinear part of the curve could not be fitted properly.

$Q[-]$ / F_0 [nN]	1.860	1.880	1.900	1.920	1.1940	1.960
296						14.2
297						12.6
298						10.9
299					14.2	9.5
300					12.7	
301					11.0	
302				14.4	9.6	
303				12.9		
304				11.2		
305			14.7	9.8		
306			13.1			
307			11.6			
308		15.1	10.1			
309		13.5				
310		11.9				
311		10.5				
312	14.0					
313	12.5					
314	11.0					
314	9.5					

$Q[-]$ / F_0 [nN]	1.860	1.880	1.900	1.920	1.1940	1.960
296						
297						14.0
298						12.3
299						10.7
300					14.0	9.1
301					12.3	
302					10.5	
303				14.0	9.0	
304				12.3		
305				10.7		
306			14.0	9.0		
307			12.4			
308			10.7			
309		14.2	9.2			
310		12.6				
311		11.0				
312	14.5	9.5				
313	12.8					
314	11.3					
315	9.8					

$Q[-]$ / F_0 [nN]	1.860	1.880	1.900	1.920	1.1940	1.960
296						
297						16.5
298						13.6
299						11.9
300					15.3	10.2
301					13.5	
302					11.7	
303				15.0	9.9	
304				13.3		
305				11.5		
306			15.0	9.8		
307			13.2			
308			11.4			
309		15.0	9.8			
310		13.2				
311		11.5				
312	15.0	9.8				
313	13.3					
314	11.5					
315	9.9					

B.5. Irregularities in the Frequency Response

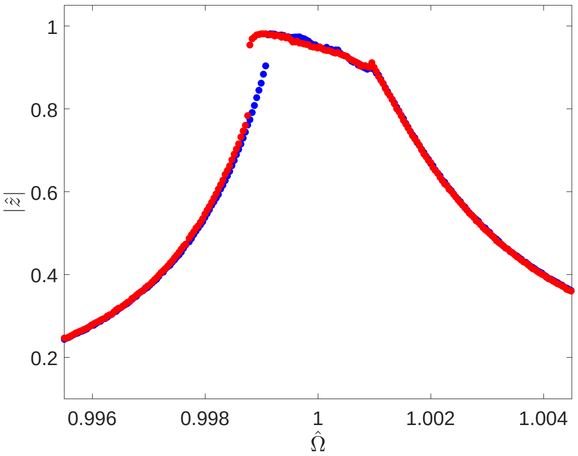

Figure B.7: Experimental forward (blue dots) and backward (red dots) frequency response curves of two different NCLR cantilevers with softening nonlinearity. The height and width of these curves are difficult to fit, due to the discrepancy between the outer parts of the curves.

It was observed that the response of some cantilevers was somewhat irregular, even linear frequency response curves without softening or hardening were difficult to match with numerical simulations. The asymmetry in the curves of Fig. B.7 could be related to improper position of the laser, imperfect mounting of the cantilever on the scan head or irregularities in its geometry. The fitting procedure is difficult to apply when the cantilever response is noticeably affected, as the model assumes symmetry in the shape, and it does not yet incorporate the physical effects of laser positioning and cantilever mounting on the frequency response.

B.6. Backbone Curves Indicating Drift in z_c

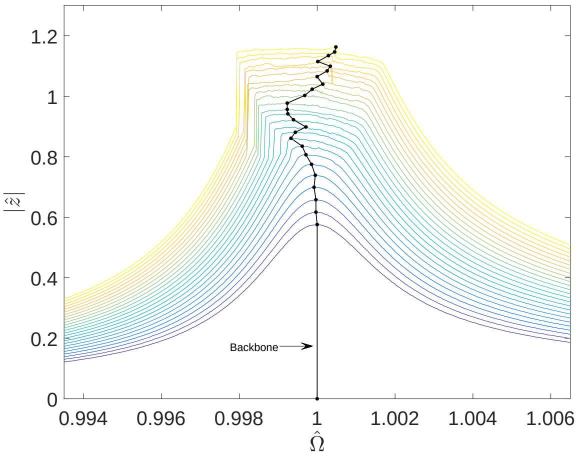

Figure B.8: Experimental backbone curve obtained with the 'tip lift' procedure, performed on a mica sample, $z_c \approx 30\,\text{nm}$. The backbone indicates that the cantilever base moves away from the sample

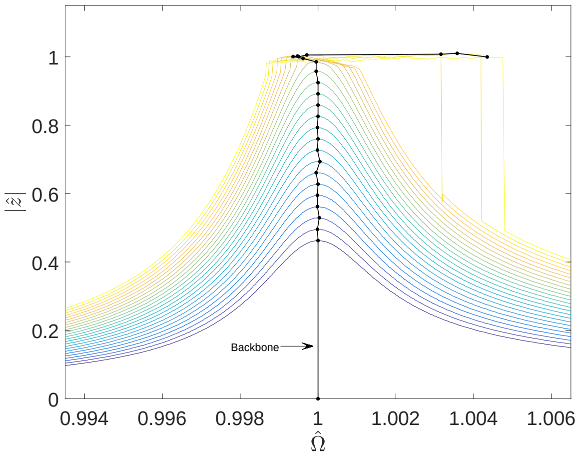

Figure B.9: Experimental backbone curve obtained with the 'tip lift' procedure, performed on a mica sample, $z_c \approx 30\,\text{nm}$. The backbone indicates that the cantilever base moves towards the sample in the repulsive regime.

The backbone curves from the sequential frequency sweeps shows softening turning into hardening. The force steps can be controlled very accurately, as can be in observed in the plot. Due to the fact that the Z-controller is switched off during the second scan the cantilever base is free to be influenced by external effects, causing drift in the Z-direction. Especially when the scan time is increased, the drift increases. In Fig. B.8, the amplitude continues to increase even when the sample is reached (characterized by the hardening), which indicates that the cantilever base is retracting from the sample. In Fig. B.9, it is the other way around. The backbone shows a short softening turning into hardening, with in the end a decrease in the amplitude, which indicates that the base-sample distance has decreased.

C

Supplementary Information

C.1. Preparing an Experiment

C.1.1. Cantilever Mounting

For each experiment, the laser needs to be placed on the correct position on the cantilever. The cantilever holder of the FLEX AFM ensures that the compatible cantilevers are always positioned in the same manner, even after cantilever exchange. There are grooves in the holder which ensure that compatible cantilevers are always identically aligned. In order to verify that the cantilever is placed properly on the holder, one can tap carefully on the chip with tweezers. If the cantilever moves, it is not inserted correctly, see Fig. C.1. After correct mounting the tweezers can be used to push the clipping mechanics which holds the cantilever in place.

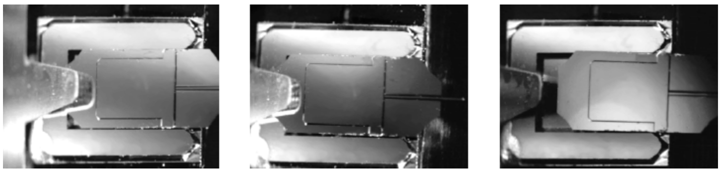

Figure C.1: LEFT: Correct alignment of the cantilever chip on the holder. CENTER & RIGHT: Incorrect alignment (source: FLEX AFM operating manual).

C.1.2. Laser Alignment

The FLEX AFM comes with 4 holes in its top cover, see Fig. C.3, that provide access to alignment screws that change different aspects of the laser beam's optical pathway. With a small key the screws in the holes can be turned in order to modify the mirror angles.

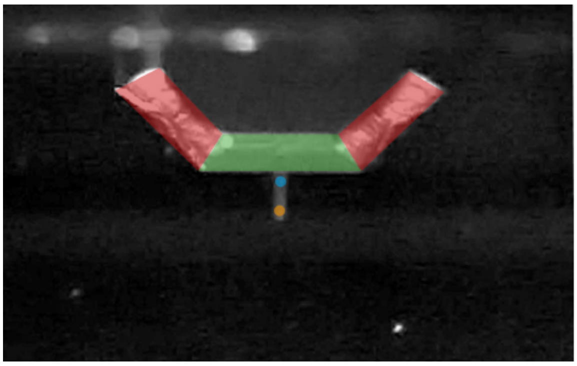

Figure C.2: Aligning the laser on the cantilever should start from the base edge (green area), followed by lateral centering on the cantilever (blue dot), and should finish near the tip end (orange dot)(source: FLEX AFM operating manual).

The laser alignment should always be carried out in the following order:

1. Identify the current laser position (screw 1 & 2);
2. Locate the base edge of the cantilever chip (screw 1 & 2);
3. Align the laser in the lateral center of the cantilever (screw 1 & 2);
4. Position the laser near the tip end (screw 1 & 2);
5. Center the laser on the photodetector (screw 3 & 4).

The centering of the laser on the photodetector is done by checking the laser alignment dialog, which displays the current position of the AFM laser spot on the photodetector and the used laser power (see Fig. C.4).

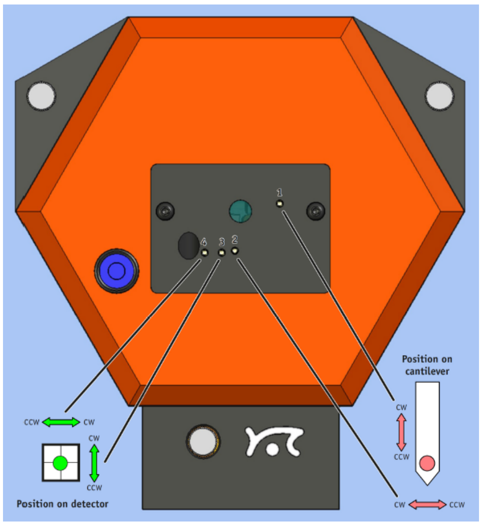

Figure C.3: Schematic top view of the FLEX AFM, indicating the 4 holes with the screws, which can be adjusted to align the laser (source: FLEX AFM operating manual).

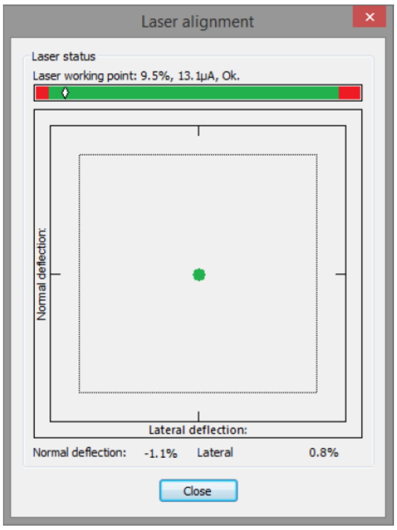

Laser working point: 9.5%, 13.1µA, Ok.

Normal deflection: -1.1% Lateral 0.8%

Figure C.4: The laser alignment dialog, displaying the current position of the laser spot on the detector (green dot) (source: FLEX AFM operating manual).

It was found in some cases a laser spot which was approved in the laser alignment dialog is not always optimal. The non-invasive calibration method in the MLA was used to check that the cantilever amplitude has a decent signal to noise ratio.

C.1.3. Calibrations

The thermal tuning dialog in the controller software can be used to determine the spring constant and resonance frequency of the cantilever. The dialog (displayed in Fig. C.5) is also useful for checking noise sources and the overall performance of the AFM scan head.

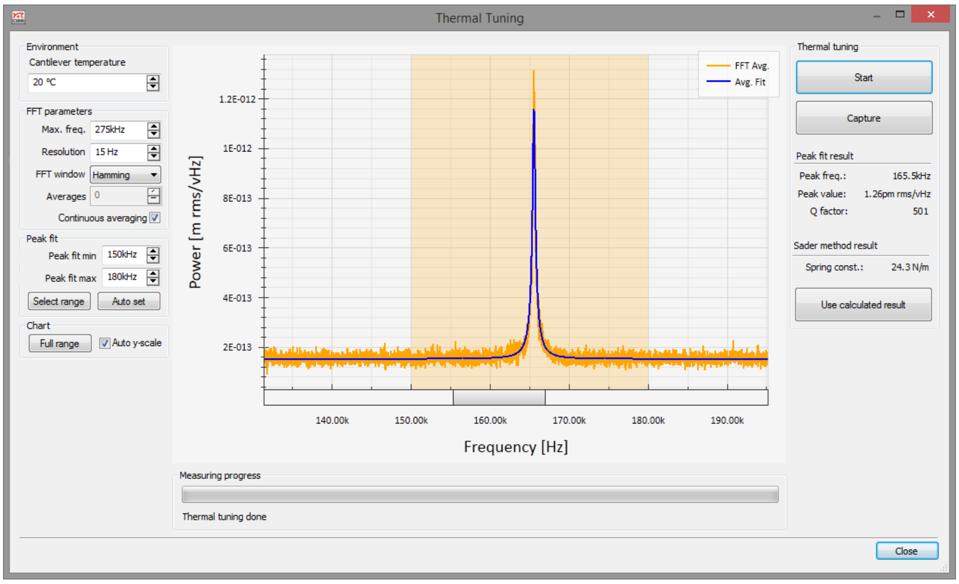

Environment
Cantilever temperature: 20 °C

FFT parameters
Max. freq. 275kHz
Resolution 15 Hz
FFT window Hamming
Averages 0
Continuous averaging ☑

Peak fit
Peak fit min 150kHz
Peak fit max 180kHz

Chart
☑ Auto y-scale

Thermal tuning

Peak fit result
Peak freq.: 165.5kHz
Peak value: 1.26pm rms/√Hz
Q factor: 501

Sader method result
Spring const.: 24.3 N/m

Measuring progress
Thermal tuning done

Figure C.5: Thermal tuning dialog of the controller software.

The calibration in the MLA is similar to the AFM calibration and relies on the same principle. Because the measurements were acquired with the MLA, the cantilevers were calibrated by that system as well. There was often a slight discrepancy in the stiffness and quality factor between the two calibrations, due to so far unknown reasons. Therefore, it was made sure that the operations carried out within the FLEX AFM were carried out with calibrated values done in the AFM software. The experimental frequency response curves were evaluated based on the calibrations of the MLA.

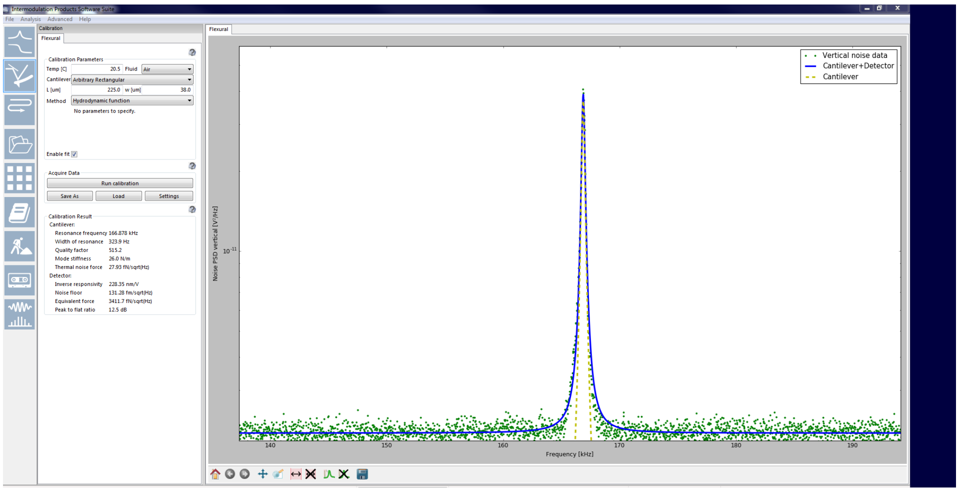

Calibration Parameters
Temp [C] 20.5 Fluid Air
Cantilever Arbitrary Rectangular
L [um] 225.0 w [um] 38.0
Method Hydrodynamic function
No parameters to specify.
Enable fit ☑

Acquire Data

Calibration Result
Cantilever:
Resonance frequency 166.878 kHz
Width of resonance 323.9 Hz
Quality factor 515.2
Mode stiffness 26.0 N/m
Thermal noise force 27.93 fN/sqrt(Hz)
Detector:
Inverse responsivity 228.35 nm/V
Noise floor 131.28 fm/sqrt(Hz)
Equivalent force 3411.7 fN/sqrt(Hz)
Peak to flat ratio 12.5 dB

Figure C.6: Thermal tuning dialog of the MLA.

For the static approach step in the systematic procedure, discussed in Chapter 4 a deflection calibration needs to be carried out. This calibration uses several spectroscopy measurements to find the deflection sensitivity of the cantilever. This procedure needs to be performed with great care, since excessive indentation will cause unwanted tip deterioration. The start point and the range of the Z-scanner position need to be chosen carefully to avoid burying the tip too deep in the sample.

C.2. Cantilever Specifications

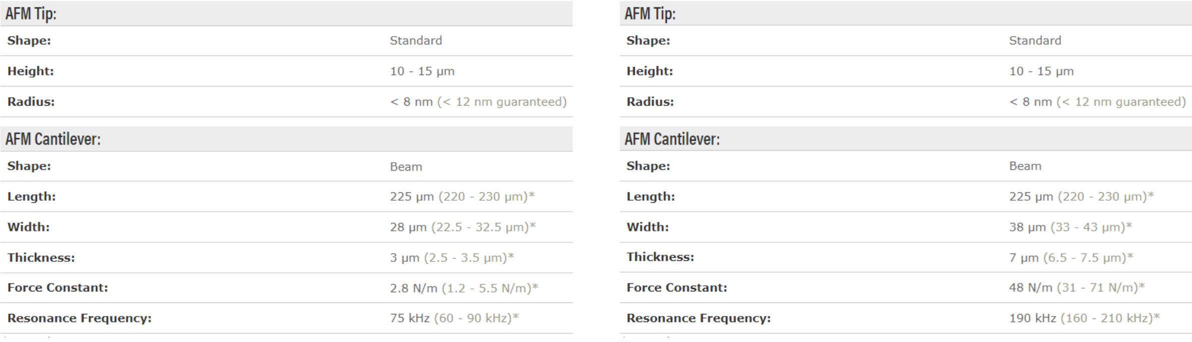

AFM Tip:	
Shape:	Standard
Height:	10 - 15 µm
Radius:	< 8 nm (< 12 nm guaranteed)

AFM Cantilever:	
Shape:	Beam
Length:	225 µm (220 - 230 µm)*
Width:	28 µm (22.5 - 32.5 µm)*
Thickness:	3 µm (2.5 - 3.5 µm)*
Force Constant:	2.8 N/m (1.2 - 5.5 N/m)*
Resonance Frequency:	75 kHz (60 - 90 kHz)*

AFM Tip:	
Shape:	Standard
Height:	10 - 15 µm
Radius:	< 8 nm (< 12 nm guaranteed)

AFM Cantilever:	
Shape:	Beam
Length:	225 µm (220 - 230 µm)*
Width:	38 µm (33 - 43 µm)*
Thickness:	7 µm (6.5 - 7.5 µm)*
Force Constant:	48 N/m (31 - 71 N/m)*
Resonance Frequency:	190 kHz (160 - 210 kHz)*

Figure C.7: Specification sheets of the AFM cantilevers used in this work, LEFT: FMR cantilever. RIGHT: NCLR cantilever (source: `https://www.nanoandmore.com/`.

Bibliography

[1] E. Rull Trinidad, T. W. Gribnau, P. Belardinelli, U. Staufer, and F. Alijani. Nonlinear dynamics for estimating the tip radius in atomic force microscopy. *Applied Physics Letters*, 111(12):1–4, 2017.

[2] Joost W. van Honschoten, Nataliya Brunets, and Niels R. Tas. Capillarity at the nanoscale. *Chemical Society Reviews*, 39(3):1096, 2010.

[3] R García. *Dynamic atomic force microscopy methods*, volume 47. 2002.

[4] Hans Jürgen Butt, Brunero Cappella, and Michael Kappl. Force measurements with the atomic force microscope: Technique, interpretation and applications. *Surface Science Reports*, 59(1-6):1–152, 2005.

[5] G. Binnig and C. F. Quate. Atomic Force Microscope. *Physical Review Letters*, 56(9):930–933, 1986.

[6] Y. Martin, C. C. Williams, and H. K. Wickramasinghe. Atomic force microscope-force mapping and profiling on a sub 100-Å scale. *Journal of Applied Physics*, 61(10):4723–4729, 1987.

[7] A. S. Lea, A. Pungor, V. Hlady, J. D. Andrade, J. N. Herron, and E. W. Voss. Manipulation of Proteins on Mica by Atomic Force Microscopy. *Langmuir*, 8(1):68–73, 1992.

[8] T Junno, K. Deppert, L. Montelius, and L. Samuelson. Controlled manipulation of nanoparticles with an atomic force microscope. *Appl. Phys. Lett.*, 66(26):3627–3629, 1995.

[9] Manfred Radmacher. Measuring the elastic properties of biological samples with the AFM. *IEEE Engineering in Medicine and Biology Magazine*, 16(2):47–57, 1997.

[10] Nader Jalili and Karthik Laxminarayana. A review of atomic force microscopy imaging systems: Application to molecular metrology and biological sciences. *Mechatronics*, 14(8):907–945, 2004.

[11] Yoshiaki Sugimoto, Pablo Pou, Masayuki Abe, Pavel Jelinek, Rubén Pérez, Seizo Morita, and Óscar Custance. Chemical identification of individual surface atoms by atomic force microscopy. *Nature*, 446(7131):64–67, 2007.

[12] Georg Schitter, Juergen Steininger, Friedjof C.A. Heuck, and Urs Staufer. Towards fast AFM-based nanometrology and nanomanufacturing. *International Journal of Nanomanufacturing*, 8(5/6):392, 2012.

[13] Álvaro San Paulo and Ricardo García. Unifying theory of tapping-mode atomic-force microscopy. *Physical Review B*, 66(4):041406, 2002.

[14] Franz J. Giessibl. Advances in atomic force microscopy. *Reviews of Modern Physics*, 75(3):949–983, 2003.

[15] Heinrich Hertz. On the contact of rigid elastic solids. *Journal fur die Reine und Angewandte Mathematik*, 1882(92):156–171, 1882.

[16] K. L. Johnson, K. Kendall, and A. D. Roberts. Surface Energy and the Contact of Elastic Solids. *Proceedings of the Royal Society A: Mathematical, Physical and Engineering Sciences*, 324(1558):301–313, 1971.

[17] B V Derjaguin, V M Muller, and Y U P Toporov. Effect of contact deformation on the adhesion of particles. *Journal of colloid and interface science*, 52(3):105–108, 1975.

[18] Daniel Maugis. Adhesion of spheres: The JKR-DMT transition using a dugdale model. *Journal of Colloid And Interface Science*, 150(1):243–269, 1992.

[19] Sang Joon Cho, Byung Woon Ahn, Joonhui Kim, Jung Min Lee, Yueming Hua, Young K. Yoo, and Sang Il Park. Three-dimensional imaging of undercut and sidewall structures by atomic force microscopy. *Review of Scientific Instruments*, 82(2):1–6, 2011.

[20] Ndubuisi G. Orji, Hiroshi Itoh, Chumei Wang, Ronald G. Dixson, Peter S. Walecki, Sebastian W. Schmidt, and Bernd Irmer. Tip characterization method using multi-feature characterizer for CD-AFM. *Ultramicroscopy*, 162:25–34, 2016.

[21] Robert W. Stark. Bistability, higher harmonics, and chaos in AFM. *Materials Today*, 13(9):24–32, 2010.

[22] Yang Gan. Atomic and subnanometer resolution in ambient conditions by atomic force microscopy. *Surface Science Reports*, 64(3):99–121, 2009.

[23] Jeffrey L. Hutter and John Bechhoefer. Calibration of atomic-force microscope tips. *Review of Scientific Instruments*, 64(7):1868–1873, 1993.

[24] John E Sader, Ian Larson, Paul Mulvaney, and Lee R White. Method for the calibration of atomic force microscope cantilevers. *Rev. Sci. Instrum.*, 66(7):3789–3798, 1995.

[25] Gerhard Meyer and Nabil M. Amer. Erratum: Novel optical approach to atomic force microscopy [Appl. Phys. Lett. 5 3 , 1045 (1988)]. *Applied Physics Letters*, 53(24):2400–2402, 1988.

[26] Gerhard Meyer and Nabil M. Amer. Optical-beam-deflection atomic force microscopy: The NaCl (001) surface. *Applied Physics Letters*, 56(21):2100–2101, 1990.

[27] T. R. Albrecht, P. Grütter, D. Horne, and D. Rugar. Frequency modulation detection using high-Q cantilevers for enhanced force microscope sensitivity. *Journal of Applied Physics*, 69(2):668–673, 1991.

[28] Ricardo Garcia and Alvaro San Paulo. Attractive and repulsive tip-sample interaction regimes in tapping-mode atomic force microscopy. *Physical Review B*, 60(7):4961–4967, 1999.

[29] M. Marth, D. Maier, J. Honerkamp, R. Brandsch, and G. Bar. A unifying view on some experimental effects in tapping-mode atomic force microscopy. *Journal of Applied Physics*, 85(10):7030, 1999.

[30] Ricardo García and Alvaro San Paulo. Dynamics of a vibrating tip near or in intermittent contact with a surface. *Physical Review B*, 61(20):R13381–R13384, 2000.

[31] X Chen, M C Davies, C J Roberts, S J B Tendler, P M Williams, and N A Burnham. Optimizing phase imaging via dynamic force curves. *Surface Science*, 460(1-3):292–300, 2000.

[32] Anders Kühle, Alexis H. So/rensen, and Jakob Bohr. Role of attractive forces in tapping tip force microscopy. *Journal of Applied Physics*, 81(10):6562–6569, 1997.

[33] Lugen Wang. Analytical descriptions of the tapping-mode atomic force microscopy response. *Applied Physics Letters*, 73(25):3781–3783, 1998.

[34] S. I. Lee, S. W. Howell, A. Raman, and R. Reifenberger. Nonlinear dynamics of microcantilevers in tapping mode atomic force microscopy: A comparison between theory and experiment. *Physical Review B*, 66(11):115409, 2002.

[35] Robert W. Stark, Georg Schitter, and Andreas Stemmer. Tuning the interaction forces in tapping mode atomic force microscopy. *Physical Review B*, 68(8):085401, 2003.

[36] S. I. Lee, S. W. Howell, A. Raman, and R. Reifenberger. Nonlinear dynamic perspectives on dynamic force microscopy. *Ultramicroscopy*, 97(1-4):185–198, 2003.

[37] S. Rutzel, S. I. Lee, and A. Raman. Nonlinear dynamics of atomic-force-microscope probes driven in Lennard-Jones potentials. *Proceedings of the Royal Society A: Mathematical, Physical and Engineering Sciences*, 459(2036):1925–1948, 2003.

[38] R. Hillenbrand, M. Stark, and R. Guckenberger. Higher-harmonics generation in tapping-mode atomic-force microscopy: Insights into the tip–sample interaction. *Applied Physics Letters*, 76(23):3478–3480, 2000.

[39] Ozgur Sahin, Calvin F. Quate, Olav Solgaard, and Abdullah Atalar. Resonant harmonic response in tapping-mode atomic force microscopy. *Physical Review B - Condensed Matter and Materials Physics*, 69(16):1–9, 2004.

[40] M. Balantekin and A. Atalar. Enhancing higher harmonics of a tapping cantilever by excitation at a submultiple of its resonance frequency. *Physical Review B - Condensed Matter and Materials Physics*, 71(12):1–6, 2005.

[41] S. Crittenden, A. Raman, and R. Reifenberger. Probing attractive forces at the nanoscale using higher-harmonic dynamic force microscopy. *Physical Review B - Condensed Matter and Materials Physics*, 72(23):1–13, 2005.

[42] Koo Hyun Chung, Yong Ha Lee, and Dae Eun Kim. Characteristics of fracture during the approach process and wear mechanism of a silicon AFM tip. *Ultramicroscopy*, 102(2):161–171, 2005.

[43] Jingjing Liu, Jacob K. Notbohm, Robert W. Carpick, and Kevin T. Turner. Method for characterizing nanoscale wear of atomic force microscope tips. *ACS Nano*, 4(7):3763–3772, 2010.

[44] Tevis D. B. Jacobs and Robert W. Carpick. Nanoscale wear as a stress-assisted chemical reaction. *Nature Nanotechnology*, 8(2):108–112, 2013.

[45] Koo Hyun Chung. Wear characteristics of atomic force microscopy tips: A reivew. *International Journal of Precision Engineering and Manufacturing*, 15(10):2219–2230, 2014.

[46] J S Villarrubia. Algorithms for scanned probe microscope image simulation, surface reconstruction, and tip estimation. *Journal of Research of the National Institute of Standards and Technology*, 102(4):425, 1997.

[47] Fenglei Tian, Xiaoping Qian, and J. S. Villarrubia. Blind estimation of general tip shape in AFM imaging. *Ultramicroscopy*, 109(1):44–53, 2008.

[48] L. S. Dongmo, J. S. Villarrubia, S. N. Jones, T. B. Renegar, M. T. Postek, and J. F. Song. Experimental test of blind tip reconstruction for scanning probe microscopy. *Ultramicroscopy*, 85(3):141–153, 2000.

[49] J. Liu, D. S. Grierson, N. Moldovan, J. Notbohm, S. Li, P. Jaroenapibal, S. D. O'Connor, A. V. Sumant, N. Neelakantan, J. A. Carlisle, K. T. Turner, and R. W. Carpick. Preventing nanoscale wear of atomic force microscopy tips through the use of monolithic ultrananocrystalline diamond probes. *Small*, 6(10):1140–1149, 2010.

[50] C. Argento and R. H. French. Parametric tip model and force–distance relation for Hamaker constant determination from atomic force microscopy. *Journal of Applied Physics*, 80(11):6081–6090, 1996.

[51] Sergio Santos, Li Guang, Tewfik Souier, Karim Gadelrab, Matteo Chiesa, and Neil H. Thomson. A method to provide rapid in situ determination of tip radius in dynamic atomic force microscopy. *Review of Scientific Instruments*, 83(4), 2012.

[52] Shuiqing Hu, Stephen Howell, Arvind Raman, Ron Reifenberger, and Matthew Franchek. Frequency Domain Identification of Tip-sample van der Waals Interactions in Resonant Atomic Force Microcantilevers. *Journal of Vibration and Acoustics*, 126(3):343, 2004.

[53] B. Gady, D. Schleef, R. Reifenberger, D. Rimai, and L. P. DeMejo. Identification of electrostatic and van der Waals interaction forces between a micrometer-size sphere and a flat substrate. *Physical Review B*, 53(12):8065–8070, 1996.

[54] Franz J. Giessibl. Forces and frequency shifts in atomic-resolution dynamic-force microscopy. *Physical Review B*, 56(24):16010–16015, 1997.

[55] Jacob Israelachvili. *Intermolecular and Surface Forces.* 2011.

[56] B. V. Derjaguin. Untersuchungen über Die Reibung und Adhäsion. *Kolloid Zeitschrift*, 69:55–164, 1934.

[57] R Perez, I Stich, M C Payne, and K Terakura. Surface-tip interactions in noncontact atomic-force microscopy on reactive surfaces: Si(111). *Physical Review B*, 58(16):10835–10849, 1998.

[58] Igor Yu Sokolov. On the limits of the spectroscopic ability of AFM and the interaction between an AFM tip and a sample. *Surface Science*, 311(3):287–294, 1994.

[59] D Ebeling, D van den Ende, and F Mugele. Electrostatic interaction forces in aqueous salt solutions of variable concentration and valency. *Nanotechnology*, 22(30):305706, 2011.

[60] a Baratoff and P Inder. Theoretical study of short and long range forces and atom transfer in scanning force microscopy. *Physical Review B*, 46(16):10411–10421, 1992.

[61] Joonkyung Jang, George C. Schatz, and Mark A. Ratner. Capillary force in atomic force microscopy. *Journal of Chemical Physics*, 120(3):1157–1160, 2004.

[62] Ricardo Garcia, Montserrat Calleja, and Heinrich Rohrer. Patterning of silicon surfaces with noncontact atomic force microscopy: Field-induced formation of nanometer-size water bridges. *Journal of Applied Physics*, 86(4):1898–1903, 1999.

[63] K L Johnson and J A Greenwood. An Adhesion Map for the Contact of Elastic Spheres. *Journal of Colloid and Interface Science*, 192(2):326–333, 1997.

[64] Eusebius J. Doedel and Bart E. Oldeman. AUTO-07P : CONTINUATION AND BIFURCATION SOFTWARE FOR ORDINARY DIFFERENTIAL EQUATIONS, 2013.

[65] Hans-Jürgen Butt and Manfred Jaschke. Calculation of thermal noise in atomic force microscopy. *Nanotechnology*, 6:1–7, 1995.

[66] Robert W Stark and Wolfgang M Heckl. Fourier transformed atomic force microscopy: tapping mode atomic force microscopy beyond the Hookian approximation. 457:219–228, 2000.

[67] Christopher P. Green and John E. Sader. Torsional frequency response of cantilever beams immersed in viscous fluids with applications to the atomic force microscope. *Journal of Applied Physics*, 92(10):6262–6274, 2002.

[68] Dror Sarid. Driven nonlinear atomic force microscopy cantilevers: From noncontact to tapping modes of operation. *Journal of Vacuum Science & Technology B: Microelectronics and Nanometer Structures*, 14(2):864, 1996.

[69] B. Anczykowski, D. Krüger, and H. Fuchs. Cantilever dynamics in quasinoncontact force microscopy: Spectroscopic aspects. *Physical Review B*, 53(23):15485–15488, 1996.

[70] J Tamayo and R Garcia. Deformation, Contact Time, and Phase Contrast in Tapping Mode Scanning Force Microscopy - Langmuir (ACS Publications). *Langmuir*, 7463(13):4430–4435, 1996.

[71] R. G. Winkler, J. P. Spatz, S. Sheiko, M. Möller, P. Reineker, and O. Marti. Imaging material properties by resonant tapping-force microscopy: A model investigation. *Physical Review B*, 54(12):8908, 1996.

[72] Lugen Wang. The role of damping in phase imaging in tapping mode atomic force microscopy. *Surface Science*, 429:178–185, 1999.

[73] N Sasaki, M Tsukada, R Tamura, K Abe, and N Sato. Dynamics of the cantilever in noncontact atomic force microscopy. *Applied Physics A*, 66:S287–S291, 1998.

[74] Jeffery P. Hunt and Dror Sarid. Kinetics of lossy grazing impact oscillators. *Applied Physics Letters*, 72(23):2969–2971, 1998.

[75] F Jamitzky, M Stark, W Bunk, W M Heckl, and R W Stark. Chaos in dynamic atomic force microscopy. *Nanotechnology*, 17(7):S213–S220, 2006.

[76] Willem van de Water and Jaap Molenaar. Dynamics of vibrating atomic force microscopy. *Nanotechnology*, 11(3):192–199, 2000.

[77] Greg Haugstad and Richard R. Jones. Mechanisms of dynamic force microscopy on polyvinyl alcohol: Region- specific non-contact and intermittent contact regimes. *Ultramicroscopy*, 76(1-2):77–86, 1999.

[78] Michael Reinstaedtler, Ute Rabe, Volker Scherer, Joseph A. Turner, and Walter Arnold. Imaging of flexural and torsional resonance modes of atomic force microscopy cantilevers using optical interferometry. *Surface Science*, 532-535(May 2014):1152–1158, 2003.

[79] Yaxin Song and Bharat Bhushan. Simulation of dynamic modes of atomic force microscopy using a 3D finite element model. *Ultramicroscopy*, 106(8-9):847–873, 2006.

[80] Arvind Raman, John Melcher, and Ryan Tung. Cantilever dynamics in atomic force microscopy. *Nano Today*, 3(1-2):20–27, 2008.

[81] Tomás R. Rodríguez and Ricardo García. Compositional mapping of surfaces in atomic force microscopy by excitation of the second normal mode of the microcantilever. *Applied Physics Letters*, 84(3):449–451, 2004.

[82] Ricardo Garcia and Roger Proksch. Nanomechanical mapping of soft matter by bimodal force microscopy. *European Polymer Journal*, 49(8):1897–1906, 2013.

[83] Robert W. Stark and Wolfgang M. Heckl. Higher harmonics imaging in tapping-mode atomic-force microscopy. *Review of Scientific Instruments*, 74(12):5111–5114, 2003.

[84] A. Raman, S. Trigueros, A. Cartagena, A. P. Z. Stevenson, M. Susilo, E. Nauman, and S. Antoranz Contera. Mapping nanomechanical properties of live cells using multi-harmonic atomic force microscopy. *Nature Nanotechnology*, 6(12):809–814, 2011.

[85] Martin Stark, Robert W Stark, Wolfgang M Heckl, and Reinhard Guckenberger. Spectroscopy of the anharmonic cantilever oscillations in tapping-mode atomic-force microscopy. *Applied Physics Letters*, 77(20):3293–3295, 2000.

[86] Lennart Bergström. Hamaker constants of inorganic materials. *Advances in Colloid and Interface Science*, 70:125–169, 1997.

[87] Marco Amabili, Farbod Alijani, and Joachim Delannoy. Damping for large-amplitude vibrations of plates and curved panels, part 2: Identification and comparisons. *International Journal of Non-Linear Mechanics*, 85:226–240, 2016.